PHYSICAL REVIEW D VOLUME 35, NUMBER 1 1 JANUARY 1987

Beyond leading-order perturbative QCD corrections to $\gamma\gamma \rightarrow M^+M^-$ ($M=\pi,K$)

Bene Nižić*
Newman Laboratory of Nuclear Studies, Cornell University, Ithaca, New York 14853

(Received 20 December 1985)

Next-to-leading-order perturbative QCD predictions are obtained for the two-photon exclusive channels $\gamma\gamma \rightarrow M^+M^-$ ($M=\pi,K$) at large momentum transfer. The calculation is carried out in the Feynman gauge. The dimensional-regularization method is used to control both ultraviolet and infrared divergences. The model meson distribution amplitude $\Phi_M \propto \delta(x-\frac{1}{2})$ is utilized as a candidate form for the nonperturbative dynamical input. In order to reduce the effect of the particular choice of Φ_M, similarity between $\gamma\gamma \rightarrow M^+M^-$ and $\gamma^* \rightarrow M^+M^-$ (timelike meson electromagnetic form factor) is employed. In the modified minimal-subtraction ($\overline{\text{MS}}$) scheme definition of α_s, renormalized at $W_{\gamma\gamma}$ (total center-of-mass energy of the $\gamma\gamma$ system), and with the present estimates of $\Lambda_{\overline{\text{MS}}}$ (~ 150 MeV), it is found that next-to-leading-order corrections become sufficiently small ($<25\%$) only for $W_{\gamma\gamma} > 10$ GeV, which is much larger than the highest $W_{\gamma\gamma}$ for which experimental data exist.

I. INTRODUCTION

One specific aspect of perturbative QCD which has received considerable attention in the last few years is the study of exclusive processes at large momentum transfer. This development was due to the work of Brodsky and Lepage[1] and, independently, Efremov and Radyshkin.[2] They have demonstrated systematically to all orders in perturbation theory that amplitudes for large-momentum-transfer exclusive processes factor into a hard-scattering amplitude T_H and a soft, in perturbation theory incalculable, distribution amplitude $\Phi(x_i,Q)$.

Large-momentum-transfer exclusive processes that have been analyzed within the framework established in Refs. 1 and 2 include meson and baryon electroweak form factors,[3–5] fixed-angle hadron-hadron scattering,[6] two-photon processes,[7,8] heavy-quarkonia decays,[9] and several other processes. Analyses of these processes have led to a new range of predictions which test both the scaling and spin properties of quark and gluon interactions as well as the detailed structure of hadronic wave functions at short distances.

In the area of exclusive processes, two-photon processes are of special interest since they can provide very clean tests of perturbative QCD. Owing to the pointlike structure of the photon, initial states in these reactions are simple and controllable, and strong interactions are present only in final states. This results in a substantial simplification of the analysis of these exclusive scattering amplitudes. For these processes, large-momentum-transfer scaling behavior, helicity structure, and, often, even the absolute normalization can be rigorously computed.

Photon-photon annihilation into two flavor-nonsinglet helicity-zero mesons, $\gamma\gamma \rightarrow M^+M^-$ ($M=\pi,K$), is probably one of the simplest hadronic processes and it is this process that we intend to concentrate on in this paper. In the framework set out in Refs. 1 and 2, the $\gamma_\lambda\gamma_{\lambda'} \rightarrow M^+M^-$ process at high energies and large center-of-mass scattering angles $\theta_{\text{c.m.}}$ is described by the helicity amplitudes (see Fig. 1)

$$\mathcal{M}(\lambda\lambda';s,\theta_{\text{c.m.}}) = \int_0^1 dx \int_0^1 dy\, \Phi_M^*(x,\overline{Q_x})\Phi_M^*(y,\overline{Q_y}) \times T_H(\lambda\lambda';x,y;s,\theta_{\text{c.m.}}) , \quad (1.1)$$

where $\overline{Q_x} \sim \min(x,1-x)\sqrt{s}\,|\sin\theta_{\text{c.m.}}|$ (and similarly for $\overline{Q_y}$), λ and λ' are photon helicities, and $\sqrt{s} \equiv W_{\gamma\gamma}$ is the total center-of-mass energy of the $\gamma\gamma$ system (or the invariant mass of the M^+M^- pair).

The function $\Phi_M(x,Q)$ in (1.1) is the meson distribution amplitude. The intuitive interpretation of $\Phi_M(x,Q)$ is that it represents the amplitude for the meson consisting of a $q\bar{q}$ pair, with the quark and antiquark collinear and on shell relative to the scale Q, and sharing fractions x and $1-x$ of the meson's total momentum. $\Phi_M(x,Q)$ is intrinsically nonperturbative; it contains all effects of collinear singularities, confinement, nonperturbative interactions, and meson bound-state dynamics. As far as the computation of $\Phi_M(x,Q)$ is concerned, the method based on the QCD sum rules[10] seems very promising. Eventually, one can also hope to compute $\Phi_M(x,Q)$ using lattice numerical methods[11] or directly from the QCD equations of motion.[12]

The function T_H in (1.1) is the hard-scattering ampli-

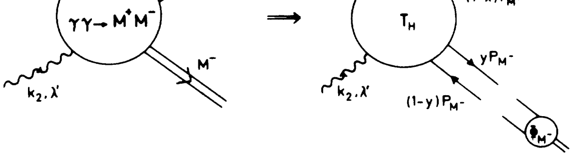

FIG. 1 Factorization of the $\gamma_\lambda\gamma_{\lambda'} \rightarrow M^+M^-$ helicity amplitude at high energies and large center-of-mass scattering angles.

tude for producing collinear meson constituents from the initial photon pair. By definition, T_H is free of collinear singularities and has a well-defined perturbative expansion in $\alpha_s(W_{\gamma\gamma})$. Thus, one can write

$$T_H(\lambda\lambda';x,y;s,\theta_{\text{c.m.}}) = \alpha_s(W_{\gamma\gamma})T_H^{(0)}(\lambda\lambda';x,y;s,\theta_{\text{c.m.}}) \times \left[1+\frac{\alpha_s(W_{\gamma\gamma})}{\pi}T_H^{(1)}(\lambda\lambda';x,y;s,\theta_{\text{c.m.}})+\cdots\right]. \tag{1.2}$$

The function T_H is obtained by evaluating the $\gamma\gamma\to(q\bar{q})+(q\bar{q})$ amplitude, which is described by the Feynman diagrams of Fig. 2, with massless quarks collinear with outgoing mesons. This neglects terms of order m^2/s, and, since the constituents are constrained to be collinear, it also neglects terms of order $k_\perp{}^2/s$, where $k_\perp$ is the average transverse momentum in the meson (typically of order 300 MeV). These terms are negligible in the limit of very large s.

As is well known, unlike in QED, the lowest-order calculations in QCD do not have much predictive power, the reason being that the perturbative QCD effective expansion parameter $\alpha_s(Q)$ does not seem small at currently accessible energies. Consequently, one must be careful before applying lowest-order QCD results to existing experimental data. It has by now been well recognized that to achieve complete confrontation between theoretical predictions and experimental results, it is crucial that higher-order corrections should be obtained.

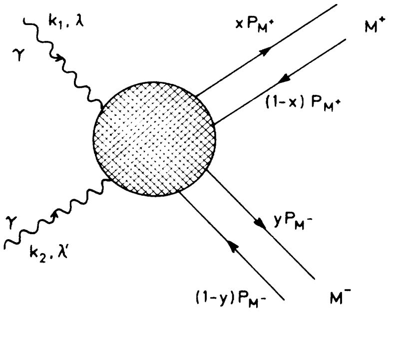

FIG. 2. Feynman diagrams describing the $\gamma\gamma\to(q\bar{q})+(q\bar{q})$ amplitude in terms of which the hard-scattering amplitude for the $\gamma\gamma\to M^+M^-$ transition is obtained.

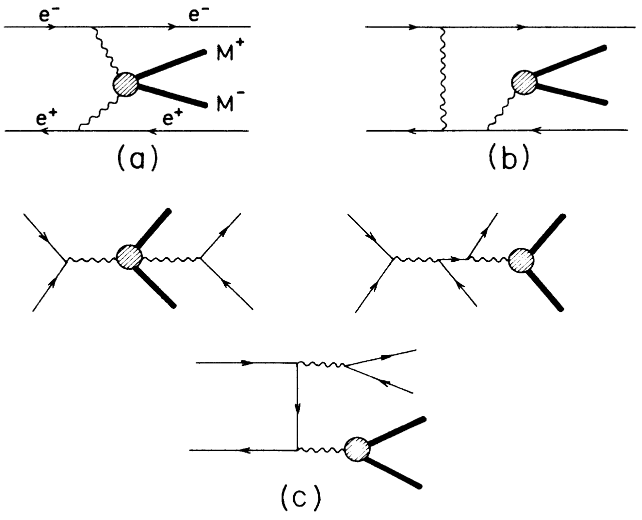

FIG. 3. Different mechanisms contributing to the $e^+e^-\to e^+e^-M^+M^-$ process in terms of which the $\gamma\gamma\to M^+M^-$ reaction can be studied: (a) two-photon production, (b) bremsstrahlung production, (c) annihilation production.

A physical process by means of which one can study the $\gamma\gamma\to M^+M^-$ transition is the $e^+e^-\to e^+e^-M^+M^-$ process. Mechanisms contributing to this process are shown in Fig. 3. Among them, the two-photon mechanism of Fig. 3(a) is the dominant one. This is due to the fact that only in this case both photon "masses" can be simultaneously small and the cross section is not suppressed by photon propagators. If one restricts himself to the region where both electron scattering angles are small, the contribution of the mechanisms shown in Figs. 3(b) and 3(c) are negligibly small and the information about the $\gamma\gamma\to M^+M^-$ cross section with both photons (quasi) real can be extracted.[13] In this case, the cross section for $e^+e^-\to e^+e^-M^+M^-$ factorizes into a $\gamma\gamma\to M^+M^-$ cross section multiplied by a $\gamma\gamma$ luminosity function as

$$\frac{d\sigma(e^+e^-\to e^+e^-M^+M^-)}{dW_{\gamma\gamma}d\Omega} = 4\left[\frac{\alpha}{\pi}\right]^2\frac{P(\xi)}{W_{\gamma\gamma}}\frac{d\sigma(\gamma\gamma\to M^+M^-)}{d\Omega}, \tag{1.3}$$

where $\xi=W_{\gamma\gamma}/2E_{\text{beam}}$, while $P(\xi)$ is the photon flux density which for untagged processes is given by[14]

$$P(\xi)=(2+\xi^2)^2\ln\frac{1}{\xi}-(1-\xi^2)(3+\xi^2). \tag{1.4}$$

The $\gamma\gamma\to M^+M^-$ $(M=\pi,K)$ process has been the subject of a number of experimental investigations. Better and better data and data at higher and higher energies are becoming available. The Mark II group at the SLAC e^+e^- storage ring SPEAR has recently reported results of the measurement of $\sigma(\gamma\gamma\to\pi^+\pi^-+K^+K^-)$ in the region $1.6\le W_{\gamma\gamma}\le 2.4$ GeV (Ref. 15). These results have now been extended to include the region $2.4\le W_{\gamma\gamma}\le 3.5$ GeV (Ref. 16), and separate $\pi^+\pi^-$ and K^+K^- contributions have been obtained.[17] The data, although statistically limited, are in reasonably good agreement with the existing lowest-order QCD prediction.

The leading-order perturbative QCD analysis of the process $\gamma\gamma\to M^+M^-$ $(M=\pi,K)$ has been performed by Brodsky and Lepage.[7] In order to check the reliability of their leading-order predictions, in this paper we examine next-to-leading-order corrections to this process.

The plan of this paper is as follows. In Sec. II we discuss some ingredients needed in the calculation. In Sec.

III we review the lowest-order predictions as originally obtained by Brodsky and Lepage.[7] In Sec. IV we present our calculation of next-to-leading-order corrections to the $\gamma\gamma\to M^+M^-$ cross section and compare our results with the currently available experimental data. Section V is devoted to some concluding remarks. As an illustration of the calculational method employed, in Appendix A we present a detailed evaluation of diagram A14 of Fig. 7. Finally, in Appendix B we describe a method suitable for numerical evaluation of the integrals containing first-order poles and which are, therefore, defined by the principal-value prescription.

II. PRELIMINARIES

A. Kinematics

The process we want to study is

$$\gamma_1(k_1,\epsilon_1^\lambda)+\gamma_2(k_2,\epsilon_2^{\lambda'})\to M^+(P_{M^+})+M^-(P_{M^-}) ,$$

where both photons are real and M stands for a flavor-nonsinglet pseudoscalar meson, such as π or K. To make the analysis of collinear divergences easier, it is convenient to choose the $\gamma\gamma$ center-of-mass frame in which the four-momenta of the incoming and outgoing particles are given by

$$\begin{aligned} &k_1=p+q, \quad k_2=p-q , \\ &P_{M^+}=p+k, \quad P_{M^-}=p-k , \end{aligned} \tag{2.1}$$

where

$$\begin{aligned} p&=\frac{\sqrt{s}}{2}(1,0,0,0) , \\ k&=\frac{\sqrt{s}}{2}(0,0,0,1) , \\ q&=\frac{\sqrt{s}}{2}(0,-\sin\theta_{\text{c.m.}},0,\cos\theta_{\text{c.m.}}) . \end{aligned} \tag{2.2}$$

Polarization states of the photons are taken to be

$$\begin{aligned} \epsilon_1^+&=-\frac{1}{\sqrt{2}}(0,\cos\theta_{\text{c.m.}},i,\sin\theta_{\text{c.m.}}) , \\ \epsilon_1^-&=\frac{1}{\sqrt{2}}(0,\cos\theta_{\text{c.m.}},-i,\sin\theta_{\text{c.m.}}) , \\ \epsilon_2^+&=\epsilon_1^-,\epsilon_2^-=\epsilon_1^+ . \end{aligned} \tag{2.3}$$

Denote by $\mathcal{M}(\lambda\lambda')$ a helicity amplitude for the process studied. Then, using Lorentz invariance and taking into account (2.1)–(2.3), one immediately finds that $\mathcal{M}(\lambda\lambda')$, as well as the contribution to it arising from any diagram, has to be of the form

$$\begin{aligned} \mathcal{M}(\lambda\lambda';s,\theta_{\text{c.m.}})=&\mathcal{M}_1(q^2,q\cdot k)(\epsilon_1^\lambda\cdot\epsilon_2^{\lambda'}) \\ &+\mathcal{M}_2(q^2,q\cdot k)(\epsilon_1^\lambda\cdot k)(\epsilon_2^{\lambda'}\cdot k) . \end{aligned} \tag{2.4}$$

Use of this relation can be made in the following way. Let G be a Feynman diagram contributing to $\gamma\gamma\to M^+M^-$ and $\overline{G}$ the diagram obtained from G by interchanging the two photon vertices. Now, denoting the contributions of these two diagrams to the helicity amplitude by $\mathcal{M}(G;\lambda\lambda')$ and $\mathcal{M}(\overline{G};\lambda\lambda')$, respectively, then, in view of (2.3) and (2.4), one obtains the relation

$$\mathcal{M}(G;\lambda\lambda';\cos\theta_{\text{c.m.}})=\mathcal{M}(\overline{G};\lambda\lambda';-\cos\theta_{\text{c.m.}}) , \tag{2.5}$$

which is true to all orders in perturbation theory.

B. Pseudoscalar projection operator

The amplitude $\overline{\Phi}(x,P_M)$, for finding a q and a $\overline{q}$ inside the meson and sharing fractions x and $1-x$ of its momentum P_M, is a 16-component object given by

$$\overline{\Phi}(x,P_M)=\sum_{\sigma,\sigma'} f_{\sigma\sigma'}u_\sigma(xP_M)\overline{v}_{\sigma'}((1-x)P_M) . \tag{2.6}$$

Requiring that $f_{+-}=-f_{-+}$, to ensure the pseudoscalar state, and keeping in mind that q and $\overline{q}$ have opposite intrinsic parity, it follows from (2.6) that

$$\overline{\Phi}(x,P_M)=\frac{\gamma_5\not{P}_M}{\sqrt{2}}\Phi(x) , \tag{2.7}$$

where $\Phi(x)$ differs from $\overline{\Phi}(x)$ in that it contains a factor $\sqrt{x(1-x)}$ coming from the normalization of the spinors.

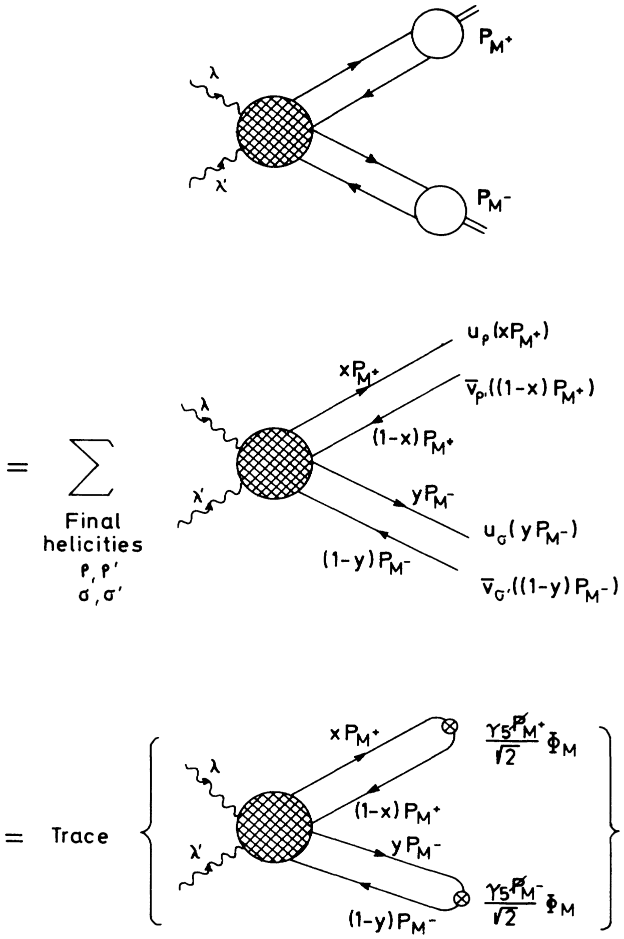

FIG. 4. Projecting the $q\overline{q}$ pair into a pseudoscalar state.

Having represented the distribution amplitude in the form (2.7) (i.e., as a 4×4 matrix), one may now write the helicity amplitude for the $\gamma\gamma\to M^+M^-$ process in terms of a trace over a fermion loop. This is illustrated in Fig. 4. In particular, one can write

$$\mathcal{M}(\lambda\lambda';s,\theta_{\rm c.m.}) = \int_0^1 dx \int_0^1 dy\, \Phi^*(x)\Phi^*(y)\Delta(\lambda\lambda';x,y;s,\theta_{\rm c.m.}) \,, \tag{2.8}$$

with

$$\Delta(\lambda\lambda';x,y;s,\theta_{\rm c.m.}) = \frac{\mathrm{Tr}\left[\dfrac{\gamma_5 \not{P}_{M^+}}{\sqrt{2}} \cdots \not{\epsilon}_1^{\lambda} \cdots \not{\epsilon}_2^{\lambda'} \cdots \dfrac{\gamma_5 \not{P}_{M^-}}{\sqrt{2}}\right]}{D(x,y;s,\theta_{\rm c.m.})} \,, \tag{2.9}$$

where the dots stand for the strings of γ matrices which depend on the details inside the cross-hatched circle in Fig. 4.

In addition to be projected into a pseudoscalar state, the $q\bar{q}$ pair should also be projected into a color-singlet state and a trace over the color indices is to be understood in (2.9).

III. LEADING-ORDER PREDICTIONS

The purpose of this section is to briefly review the leading-order perturbative QCD predictions for the $\gamma\gamma\to M^+M^-$ reaction obtained in Ref. 7.

In view of (1.1) and (1.2), the lowest-order helicity amplitude for the process is given by

$$\mathcal{M}^{(0)}(\lambda\lambda';s,\theta_{\rm c.m.}) = \alpha_s \int_0^1 dx \int_0^1 dy\, \Phi_M^*(x)\Phi_M^*(y) T_H^{(0)}(\lambda\lambda';x,y;s,\theta_{\rm c.m.}) \,, \tag{3.1}$$

where the lowest-order hard-scattering amplitude $T_H^{(0)}$ is obtained by computing 20 Feynman diagrams. These diagrams can be generated, by particle interchange, from four basic diagrams shown in Fig. 5. Let [A], [B], [C], and [D] be groups of diagrams related to the lowest-order diagrams A, B, C, and D, respectively. Further, let $T_H^{(0)}[X]$ be the joint contribution to $T_H^{(0)}$ arising from the diagrams of group $[X]$ (A,B,C,D). Then, evaluating all the diagrams and introducing $T[X]$ by

$$T_H^{(0)}[X;\lambda\lambda'] = \frac{16}{3}\frac{\pi\alpha_s e^2}{s} T[X;\lambda\lambda'] \,, \tag{3.2}$$

one finds that

$$T[\mathrm{A};++] = (e_1{}^2+e_2{}^2)\frac{4a}{x(1-x)y(1-y)} \times \left[\frac{1+z^2}{1-z^2}\right] , \tag{3.3a}$$

$$T[\mathrm{A};+-] = (e_1{}^2+e_2{}^2)\frac{4(1-a)}{x(1-x)y(1-y)} \times \left[\frac{1+z^2}{1-z^2}\right] , \tag{3.3b}$$

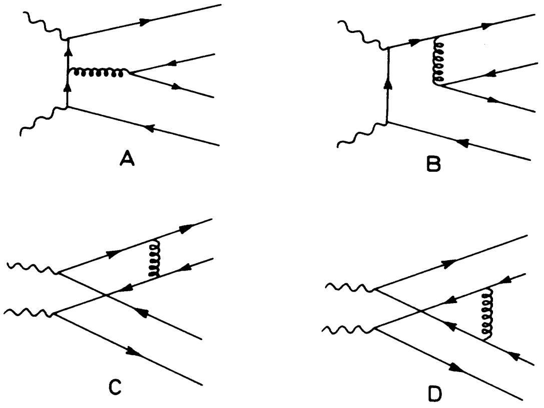

FIG. 5. Basic lowest-order diagrams for the $\gamma\gamma\to(q\bar{q})+(q\bar{q})$ amplitude. Sixteen more diagrams, which can be obtained from these by various symmetries, are not shown.

$$T[\mathrm{B};++] = (e_1{}^2+e_2{}^2)\frac{4a}{x(1-x)y(1-y)} \,, \tag{3.4a}$$

$$T[\mathrm{B};+-] = 8\frac{x(1-y)e_1{}^2+(1-x)ye_2{}^2}{x(1-x)y(1-y)} \,, \tag{3.4b}$$

$$T[\mathrm{C};++] = 2e_1e_2\frac{x(1-x)+y(1-y)}{x(1-x)y(1-y)} \times \frac{4a}{a^2-b^2z^2} \,, \tag{3.5a}$$

$$T[\mathrm{C};+-] = 2e_1e_2\frac{16a}{a^2-b^2z^2} \,, \tag{3.5b}$$

$$T[\mathrm{D};++] = \frac{-2e_1e_2}{x(1-x)y(1-y)} \times \left[\frac{8a}{1-z^2}+\frac{4a^2(1-a)}{a^2-b^2z^2}\right] , \tag{3.6a}$$

$$T[\mathrm{D};+-] = \frac{-2e_1e_2}{x(1-x)y(1-y)} \times \left[\frac{8(1-a)}{1-z^2}+\frac{4a^2(1-a)}{a^2-b^2z^2}\right] , \tag{3.6b}$$

where the following definitions have been introduced:

$$z = \cos\theta_{\rm c.m.} \tag{3.7}$$

and

$$\left.\begin{matrix} a \\ b \end{matrix}\right\} = (1-x)(1-y) \pm xy \,. \tag{3.8}$$

Now, making use of the fact that

$$\begin{aligned} &T_H^{(0)}[X;++] = T_H^{(0)}[X;--] \,, \\ &T_H^{(0)}[X;+-] = T_H^{(0)}[X;-+] \,, \\ &(X = \mathrm{A,B,C,D}) \,, \end{aligned} \tag{3.9}$$

and combining (3.2)—(3.6), one finds that

$$\left.\begin{matrix} T_H^{(0)}(++) \\ T_H^{(0)}(--) \end{matrix}\right\} = \frac{16\pi\alpha_s}{3s} \frac{32\pi\alpha}{x(1-x)y(1-y)} \left[\frac{(e_1-e_2)^2 a}{1-z^2} \right] , \tag{3.10a}$$

$$\left.\begin{matrix} T_H^{(0)}(+-) \\ T_H^{(0)}(-+) \end{matrix}\right\} = \frac{16\pi\alpha_s}{3s} \frac{32\pi\alpha}{x(1-x)y(1-y)} \left[\frac{(e_1-e_2)^2 a}{1-z^2} + \frac{e_1e_2[x(1-x)+y(1-y)]}{a^2-b^2z^2} + \frac{(e_1{}^2-e_2{}^2)(x-y)}{2} \right] . \tag{3.10b}$$

At this point one can utilize the fact that the meson distribution amplitude $\Phi_M(x,Q)$, appearing in (3.1) is universal, also occurring in other exclusive processes involving the same meson, such as its electromagnetic form factor. Assuming that $\Phi_M(x,Q)$ is symmetric in x and $1-x$, the lowest-order expression for the meson form factor takes the form

$$F_M^{(0)}(s) = \frac{16\pi\alpha_s}{3s} \int_0^1 dx \int_0^1 dy \frac{\Phi_M^*(x,Q)\Phi_M^*(y,Q)}{x(1-x)y(1-y)} . \tag{3.11}$$

Comparing (3.10) with (3.11), one notes that the x and y dependence of several terms in $T_H^{(0)}$ is very similar to that appearing in $F_M^{(0)}(s)$. This fact can be used to eliminate much of the $\Phi_M(x,Q)$ dependence from $\mathcal{M}^{(0)}(\lambda\lambda')$. With the help of (3.10) and (3.11), (3.1) can be expressed as

$$\left.\begin{matrix} \mathcal{M}^{(0)}(++) \\ \mathcal{M}^{(0)}(--) \end{matrix}\right\} = 16\pi\alpha F_M(s) \left[\frac{\langle (e_1-e_2)^2 \rangle}{1-z^2} \right] , \tag{3.12a}$$

$$\left.\begin{matrix} \mathcal{M}^{(0)}(+-) \\ \mathcal{M}^{(0)}(-+) \end{matrix}\right\} = 16\pi\alpha F_M(s) \left[\frac{\langle (e_1-e_2)^2 \rangle}{1-z^2} + 2\langle e_1e_2 \rangle \rho(z;\Phi_M) \right] . \tag{3.12b}$$

It is seen from (3.12) that all the $\Phi_M(x,Q)$ dependence of $\mathcal{M}^{(0)}(\lambda\lambda')$ is now contained in the factor $\rho(z;\Phi_M)$ which is given by the expression

$$\rho(z;\Phi_M) = \frac{\displaystyle\int_0^1 dx \int_0^1 dy \frac{\Phi_M^*(x,Q)\Phi_M^*(y,Q)}{x(1-x)y(1-y)} \frac{a[x(1-x)+y(1-y)]}{a^2-b^2z^2}}{\displaystyle\int_0^1 dx \int_0^1 dy \frac{\Phi_M^*(x,Q)\Phi_M^*(y,Q)}{x(1-x)y(1-y)}} . \tag{3.13}$$

The spin-averaged cross section is given by the relation

$$\frac{d\sigma}{dt} = \frac{2}{s}\left[\frac{d\sigma}{dz}\right] = \frac{1}{16\pi s^2}\frac{1}{4}\sum_{\lambda\lambda'} |\mathcal{M}(\lambda\lambda')|^2 . \tag{3.14}$$

Substituting (3.12) in (3.14), one finds for the lowest-order differential cross section to be

$$\left[\frac{d\sigma}{dt}\right]^{(0)} = 16\pi\alpha^2 \left|\frac{F_M(s)}{s}\right|^2 \left[\frac{\langle (e_1-e_2)^2 \rangle}{(1-z^2)^2} + \frac{2\langle e_1e_2\rangle\langle (e_1-e_2)^2\rangle}{1-z^2}\rho(z;\Phi_M) + 2\langle e_1e_2\rangle^2\rho^2(z;\Phi_M) \right] . \tag{3.15}$$

To complete the calculation of $(d\sigma/dt)^{(0)}$, it is necessary to know the meson distribution amplitude.

In general, however, $\Phi_M(x,Q)$ is an unknown function. Nevertheless, it has been shown that the leptonic decay of each meson normalizes its distribution amplitude by the "sum rule"

$$\int_0^1 dx\, \Phi_M(x,Q) = \frac{f_M}{2\sqrt{n_c}} , \tag{3.16}$$

independent of Q. In (3.16), f_M is the meson decay constant[18] and $n_c(=3)$ is the number of QCD colors. Although $\Phi_M(x,Q)$ cannot be deduced from perturbation theory, it satisfies an evolution equation of the form

$$\frac{1}{2}Q\frac{\partial}{\partial Q}\Phi_M(x,Q) = \int_0^1 dy\, V(x,y,Q)\Phi_M(y,Q) , \tag{3.17}$$

in which the evolution kernel V is calculable perturbatively. Then, given the initial condition $\Phi_M(x,Q_0)$, perturbation theory determines the evolution of $\Phi_M(x,Q)$ for $Q > Q_0$. The solution of (3.17), to leading order in $\alpha_s(Q)$, is given by[1]

$$\Phi_M(x,Q) = x(1-x)\sum_{n=0}^{\infty} a_n(Q_0{}^2)C_n^{3/2}(1-2x)\left[\ln\frac{Q^2}{\Lambda^2}\right]^{-\gamma_n} , \tag{3.18}$$

where $C_n^{3/2}(y)$ are Gegenbauer polynomials of order $\frac{3}{2}$, Λ is the characteristic QCD energy scale, and γ_n are the nonsinglet anomalous dimensions. In the limit $Q^2 \to \infty$, the solution (3.18) evolves into the form

$$\Phi_M(x,Q) \underset{Q\to\infty}{\longrightarrow} \sqrt{3} f_M x(1-x) \; . \qquad (3.19)$$

However, with increasing Q^2, this evolution is very slow (logarithmic) and, at the present-day energies, Φ_M might be different in form.

In order to see to what extent the form of Φ_M influences the prediction for the cross section of the process under consideration, we use the normalized distribution amplitude of the general form

$$\Phi_M(x,Q) = \frac{f_M}{2\sqrt{3}} \frac{\Gamma(2+2\eta)}{\Gamma^2(1+\eta)} x^{\eta}(1-x)^{\eta}, \quad \eta > 0 \; , \qquad (3.20)$$

where large $\eta(Q)$ implies a sharply peaked distribution (at $x=\frac{1}{2}$), $\eta(Q)=1$ gives the asymptotic distribution (3.19), while $\eta(Q)$ small gives a broad distribution.

The lowest-order spin-averaged cross section for $\gamma\gamma\to\pi^+\pi^-$ is plotted in Fig. 6 for three different choices of the parameter η in (3.20). Curves (a), (b), and (c) correspond to $\eta=\frac{1}{4}$, 1, and ∞, respectively. The pion form factor has been approximated by $F_\pi(s)=0.4\ \mathrm{GeV}^2/s$. As is seen from Fig. 5, the lowest-order cross section for $\gamma\gamma\to\pi^+\pi^-$ is essentially independent of the choice of Φ_M.

Given predictions for $\gamma\gamma\to\pi^+\pi^-$, predictions for $\gamma\gamma\to K^+K^-$ can be obtained using the relation

$$\frac{\dfrac{d\sigma}{dt}(\gamma\gamma\to K^+K^-)}{\dfrac{d\sigma}{dt}(\gamma\gamma\to\pi^+\pi^-)} = \left[\frac{f_K}{f_\pi}\right]^4 , \qquad (3.21)$$

which is true to all orders in α_s provided that the distribution amplitudes Φ_π and Φ_K are similar in shape.

IV. NEXT-TO-LEADING-ORDER PREDICTIONS

To obtain the complete next-to-leading-order prediction for the $\gamma\gamma\to M^+M^-$ ($M=\pi,K$) reaction, we need to calculate the corrections to both the hard-scattering amplitude and the evolution kernel for the meson distribution amplitude. In this paper we calculate only the correction to the hard-scattering amplitude. This approximation of neglecting the correction to the evolution kernel can be justified on the grounds that most of the Q dependence is contained in the hard-scattering amplitude and that the meson distribution amplitude varies slowly with changing Q.

A. Diagrams to be evaluated

Altogether there are 448 one-loop Feynman diagrams contributing to the hard-scattering amplitude T_H for the $\gamma\gamma\to M^+M^-$ process. All these diagrams can be generat-

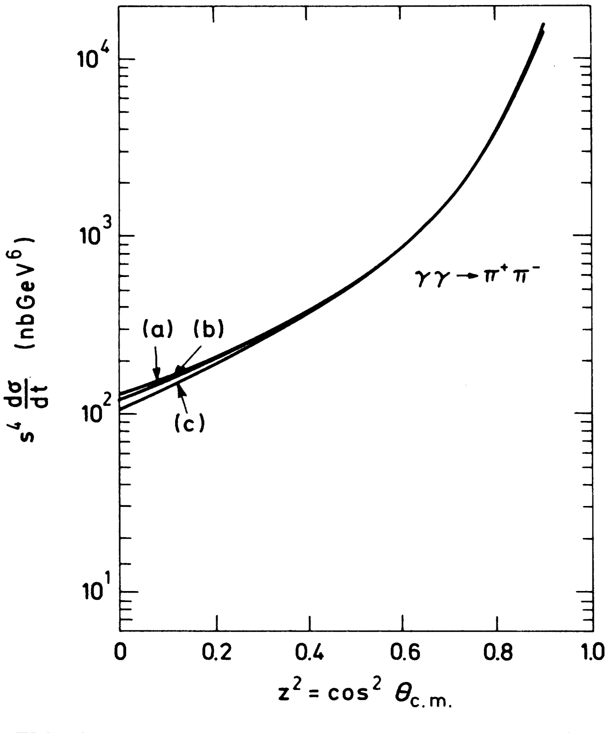

FIG. 6. Lowest-order perturbative QCD predictions for the $\gamma\gamma\to M^+M^-$ differential cross section. Curves (a), (b), and (c) correspond to the pion distribution amplitude of the form $\Phi_\pi(x,Q)\propto x(1-x)$, $|x(1-x)|^{1/4}$, and $\delta(x-\frac{1}{2})$, respectively. The pion form factor has been parametrized by $F_\pi(s)=(0.4\ \mathrm{GeV}^2)/s$.

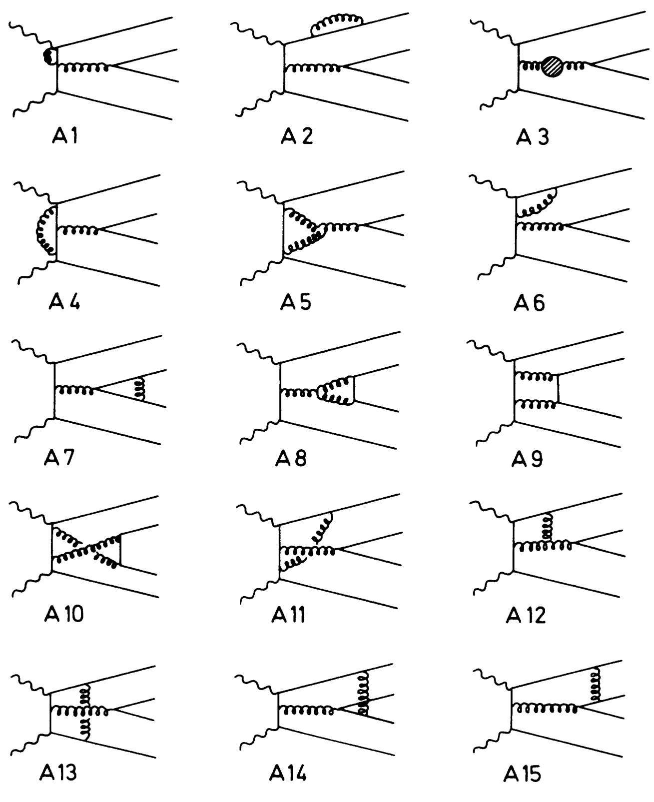

FIG. 7. Distinct one-loop diagrams of group A contributing to the $\gamma\gamma\to(q\bar{q})+(q\bar{q})$ amplitude. The total number of diagrams in this group is 104.

ed from four basic lowest-order diagrams shown in Fig. 5 by inserting an internal gluon line, interchanging particles, and taking into account diagrams with the photons crossed. Depending on which basic diagram they are related to, we divide them into four groups A, B, C, and D, containing 104, 172, 94, and 78 diagrams, respectively. Distinct diagrams from each of the four groups are shown in Figs. 7—10.

When evaluating these diagrams, one comes across ultraviolet (UV) and infrared (IR) (both collinear and soft) singularities. Recall the circumstances under which IR singularities appear. When an on-shell quark of momentum p emits a gluon of momentum k, then IR singularities appear as a result of vanishing of the quark propagator $k^2-2p\cdot k$. If the quark is massless, this can happen when either p and k are collinear ($k\,||\,p$, collinear singularity) or when the gluon momentum vanishes ($k\to 0$, soft singularity). Thus, a Feynman diagram with all particles massless and external particles being on shell will have a soft singularity if it contains an internal gluon line at-

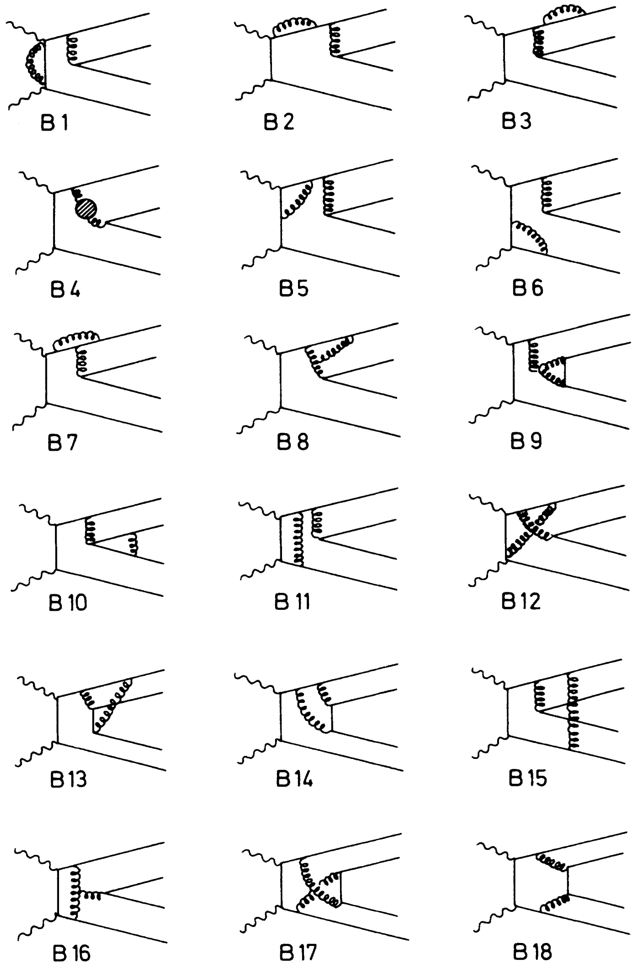

FIG. 8. Distinct one-loop diagrams of group B contributing to the $\gamma\gamma\to(q\bar{q})+(q\bar{q})$ amplitude. The total number of diagrams in this group is 172.

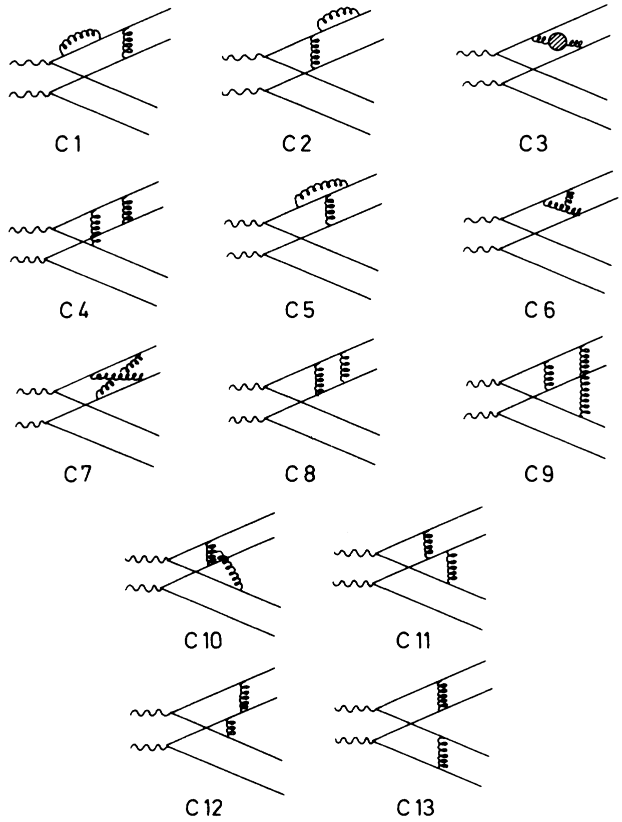

FIG. 9. Distinct one-loop diagrams of group C contributing to the $\gamma\gamma\to(q\bar{q})+(q\bar{q})$ amplitude. The total number of diagrams in this group is 94.

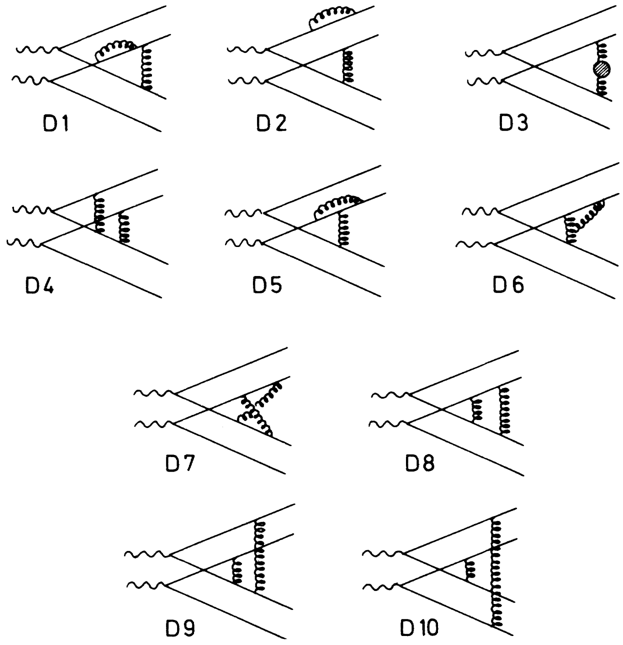

FIG. 10. Distinct one-loop diagrams of group D contributing to the $\gamma\gamma\to(q\bar{q})+(q\bar{q})$ amplitude. The total number of diagrams in this group is 78.

tached to two external quark lines. On the other hand, a diagram will contain a collinear singularity if it has an internal gluon line attached to an external quark line. It follows then that a diagram containing a soft singularity at the same time contains two collinear singularities, i.e., soft and collinear singularities overlap.

The singularities, both UV and IR, appear in every possible combination. Here are representative lists of diagrams for each combination:

UV: A4,B5,C1,D3, . . . ,

UV+collinear: A6,B8,C5,D4, . . . ,

UV+collinear+soft: A7,B10,

collinear: A10,B12,C7,D7, . . . ,

collinear+soft: A14,B15,C9,D8, ...

In addition to being plagued with singularities, these diagrams suffer from an extra complication; namely, because of the kinematics of the process under consideration, most of the diagrams develop cuts (two propagators going on shell simultaneously), leading to an imaginary part. Diagrams containing the cut(s) are

group A: all diagrams except A1, A2, and A6 ,

group B: all diagrams except B1, B3, and B6 ,

group C: C9 and C11 ,

group D: D8, D9, and D10 .

B. Regulating the divergences

In this subsection a rough outline is given of how to use the method of dimensional regularization to handle both UV and IR singularities simultaneously (at least to one-loop order).

The main ingredient of the dimensional-regularization method consists in making the replacement

$$(4\pi\alpha_s)\frac{d^4l}{(2\pi)^4}\to(4\pi\alpha_s)(\mu^2)^{2-(n/2)}\frac{d^nl}{(2\pi)^n}\ , \tag{4.1}$$

for each loop integral, where $n=4-2\epsilon$ is a real number, whose value can be varied continuously, and μ is an arbitrary mass parameter introduced to keep the coupling constant dimensionless. All internal momentum variables are taken to have n rather than four components, while external momenta are left as four-vectors. At the one-loop level, Feynman integrals have the form

$$\int\frac{d^nl}{(2\pi)^n}F(l,p)\ , \tag{4.2}$$

where p is used to denote all the external momenta. All algebraic manipulations to be performed on the integrand are carried out in the n-dimensional space-time using the metric

$$g_{00}=1,\ \ g_{0i}=0,\ \ g_{ij}=-\delta_{ij}\ ,$$
$$(i,j=1,2,\ldots,n-1)\ . \tag{4.3}$$

To deal with the diagrams containing spinor propagators internally, the algebra of the Dirac matrices has to be generalized to the n-dimensional space-time. Then

$$\{\gamma^\mu,\gamma^\nu\}=2g^{\mu\nu}\ , \tag{4.4}$$

where $g^{\mu\nu}$ is the metric of (4.3). When manipulating the γ matrices inside the integral, Eq. (4.4) must be adhered to; otherwise gauge invariance will be lost and incorrect results will be obtained. As is well known, dimensional regularization leads to an ambiguity when dealing with the pseudoscalar matrix γ_5. In practice, the difficulty arises in evaluating a trace containing a single γ_5. Each of our traces, however, contains two γ_5's, separated by an even number of γ matrices. Therefore, γ_5's can be eliminated from the traces (using the properties $\{\gamma_5,\gamma_\mu\}=0$ and $\gamma_5{}^2=1$) and dimensional regularization can be applied without difficulty. After the γ-matrix algebra is performed, the standard operations carried out on the integral (including translation of the integration variable, Feynman parametrization, and symmetric integration) are all allowed. The n-dimensional momentum integration is then carried out with the help of the formula

$$\int\frac{d^nl}{(2\pi)^n}\frac{(l^2)^r}{(l^2-V+i\epsilon)^m}=i\frac{(-1)^{r-m}}{(4\pi)^{n/2}}\frac{\Gamma(r+n/2)\Gamma(m-r-n/2)}{\Gamma(n/2)\Gamma(m)}\frac{1}{(V-i\epsilon)^{m-r-(n/2)}}\ . \tag{4.5}$$

After this integration has been carried out, all Feynman-parameter integrations have to be performed. All originally divergent integrals exhibit poles, single and/or double, at $\epsilon=0$, where $\epsilon=2-n/2$. The UV poles (labeled $1/\epsilon_{\rm UV}$) arise from the momentum integration. On the other hand, the IR poles, single and/or double (labeled $1/\epsilon_{\rm IR}$ and $1/\epsilon_{\rm IR}{}^2$, respectively), arise from the integrations over the Feynman parameters. (The appearance of the double IR poles $1/\epsilon_{\rm IR}{}^2$ is related to the fact that a soft divergence is always accompanied with two collinear divergences.) The crucial point here is that, at least to one-loop order, the poles break apart into a sum of $1/\epsilon_{\rm UV}$ and $1/\epsilon_{\rm IR}$ poles, while poles of the form $1/(\epsilon_{\rm UV}\epsilon_{\rm IR})$ never appear. Whenever the separation of the UV and IR poles is simple to that extent, one can imagine $\epsilon>0$ for the $1/\epsilon_{\rm UV}$ piece and $\epsilon<0$ for the $1/\epsilon_{\rm IR}$ piece without any problem.

C. Cancellation of soft singularities

According to the KLN theorem, soft singularities from radiative corrections are canceled by those coming from gluon bremsstrahlung. In the case we are considering, since mesons are assumed to be color-neutral states, it is impossible for them to radiate any color soft gluon. Therefore, in summing all diagrams that contribute to the exclusive amplitude $\gamma\gamma \to (q\bar{q})+(q\bar{q})$, originally present soft singularities have to cancel exactly.

The physical reason for this cancellation is the following. As the gluon becomes very soft, it is not able to resolve the parton structure of the meson, it "sees" the whole meson, which has no net color charge, and therefore decouples from the system.

Examining the diagrams in Figs. 7—10, it is easily found (by using the power-counting arguments or the Landau rules) that the ones containing soft singularities are (A7, A13, A14), (B10, B13, B15, B17), (C9, C11), and (D8, D9, D10). As mentioned in the preceding subsection, a soft singularity, when dimensionally regularized, leads to the double pole $1/\epsilon_{\rm IR}{}^2$. Evaluating all diagrams and adding up their contributions, all $1/\epsilon_{\rm IR}{}^2$ poles cancel. The cancellation takes place within each of the four groups. The final result for the amplitude contains only single $1/\epsilon_{\rm IR}$ and, of course, $1/\epsilon_{\rm UV}$ poles.

D. Method of calculation

In the following we outline the method used in performing the calculation. Details are presented in the Appendixes.

In order to obtain the hard-scattering amplitude for the $\gamma\gamma \to M^+M^-$ process to order $\alpha_s{}^2$, one has to compute Feynman diagrams of Figs. 7—10 with the number of propagators in the loop ranging from two (self-energy diagrams) to six (B17, B18, C13, and D10). Diagrams with two, three, and most of the diagrams with four propagators in the loop can be evaluated straightforwardly using the standard methods. On the other hand, it would be extremely difficult to obtain analytical results for the diagrams containing five and six propagators in the loop. The problem is that when dealing with this kind of diagrams, the standard method of combining denominators results in very complicated integrands which contain algebraic expressions raised to fractional powers. These parametric integrals could probably be evaluated analytically if the space-time dimensionality can be set equal to 4. This, however, cannot be done since all these diagrams contain IR singularities (soft and collinear) and diverge as $n \to 4$. An alternative approach would be to try to express each term in the numerator as a linear combination of the denominators with the aim of cancelling some denominators. This would result in replacing the original integral by a sum of scalar integrals (no powers of the loop-momentum vector in the numerator), each of which contains less denominators and is, therefore, easier to evaluate than the original one. Unfortunately, because of the large number of external vectors present in the problem (p, q, k, ϵ_1, and ϵ_2), this procedure cannot be carried out all the way and, therefore, does not lead to any simplification. Thus, in order to compute the hard-scattering amplitude for the process at hand, we are forced to combine both analytical and numerical methods.

A general one-loop Feynman integral can be written in the form

$$I = \int \frac{d^4 l}{(2\pi)^4} \frac{N(l,\{p_i\})}{D(l,\{p_i\})} , \tag{4.6}$$

where $\{p_i\}$ stands for the set of all external momenta. Suppose now that the integral I contains, say, UV and collinear singularities, coming from the integration regions for the virtual-gluon momenta given by $l \to \infty$ and $l \| p_j$ ($p_j{}^2=0$), respectively. Our strategy for evaluating this integral is as follows. Since we are using dimensional regularization to handle all divergences, we first continue the integral into n space-time dimensions. Next, we construct the UV and collinear subtraction terms (counterterms) $I_{\rm UV}$ and $I_{\rm coll}$, which are designed to approximate the integral I in the UV and collinear region, respectively. A subtraction term is supposed to be constructed in such a way that (i) it cancels the divergence of the original integral at each point of the integration region, (ii) it does not introduce any new divergences, (iii) it works well numerically, and (iv) it is simple enough to be evaluated analytically. Having constructed the subtraction terms, we can now formally represent the integral I as

$$I = (I - I_{\rm UV} - I_{\rm coll}) + (I_{\rm UV} + I_{\rm coll}) . \tag{4.7}$$

Note that the first term on the right-hand side is perfectly finite (by construction), while all the divergences are now contained in the second term. Denote these two terms by $I_{\rm fin}$ and $I_{\rm div}$, respectively. Our next aim is to evaluate these terms. The first term, being finite, can be evaluated in four space-time dimensions. The necessary γ-matrix algebra (trace evaluations) is performed using the computer program REDUCE (Ref. 19). The loop integral is evaluated by closing the l_0 contour at infinity, taking the residues of enclosed poles, and then performing the remaining three-momentum integral using the adaptive Monte Carlo integration routine VEGAS (Ref. 20). For most of the diagrams, the remaining three-momentum integral has poles $l_1, l_2, \ldots, l_n$ ($0 < l_i < \infty$), l now being the magnitude of the loop three-momentum vector. The integral is then properly defined by the principal-value prescription. Numerical evaluation of this kind of integral is known not to be straightforward; namely, no matter how many points are used to evaluate the integral, satisfactory accuracy cannot be achieved. The reason for this lies in the fact that the finiteness of the integral is a result of a nonlocal cancellation of infinite contributions coming from the opposite sides of a pole. Because of this, before putting the integral on computer, it is absolutely essential to transform the integrand in such a way that it becomes locally finite. An efficient way of accomplishing this is described in detail in Appendix B. After this transformation is performed, the numerical evaluation of $I_{\rm fin}$ is easily carried out. Finally, the last step is the analytic evaluation of $I_{\rm div}$. This is done using standard methods except that everything (γ-matrix algebra, momentum integration, and integration over Feynman parameters) has to be carried out systematically in n space-time dimensions. Using the modified minimal-subtraction ($\overline{\rm MS}$) scheme to cut off both the UV and the collinearly divergent integrals, one finds that

$$\begin{aligned}I_{\rm UV}&=I^{*}_{\rm UV}\frac{1}{\hat{\epsilon}_{\rm UV}}+I^{\rm fin}_{\rm UV}\ ,\\ I_{\rm coll}&=I^{*}_{\rm coll}\frac{1}{\hat{\epsilon}_{\rm IR}}+I^{\rm fin}_{\rm coll}\ ,\end{aligned}\tag{4.8}$$

where

$$\frac{1}{\hat{\epsilon}_{\rm UV}}=\frac{1}{\hat{\epsilon}_{\rm IR}}=\frac{1}{\epsilon}-\gamma_E+\ln 4\pi\ ,\tag{4.9}$$

with γ_E being the Euler constant. Therefore, on the basis of (4.7), (4.8), and (4.9) the final result takes the form

$$I=I^{*}_{\rm div}+I^{*}_{\rm fin}\ ,\tag{4.10}$$

where

$$\begin{aligned}I^{*}_{\rm div}&=I^{*}_{\rm UV}\frac{1}{\hat{\epsilon}_{\rm UV}}+I^{*}_{\rm coll}\frac{1}{\hat{\epsilon}_{\rm IR}}\ ,\\ I^{*}_{\rm fin}&=I_{\rm fin}+I^{\rm fin}_{\rm UV}+I^{\rm fin}_{\rm coll}\ .\end{aligned}\tag{4.11}$$

We conclude this subsection with a few remarks concerning the diagrams with quark self-energy corrections where the quark momentum P is on shell (A2, B3, C2, and D2). Since these corrections modify external legs, each of these diagrams is accompanied with a factor of $\frac{1}{2}$. In dimensional regularization, the contributions of each of these diagrams turn out to be proportional to

$$\Gamma=(P^2)^{-\epsilon}\ ,\tag{4.12}$$

and, therefore, vanishes when $P^2=0$. On closer inspection, however, one finds that this vanishing is a result of the cancellation of a UV pole with an IR pole. Thus, Γ can be represented as

$$\Gamma=\frac{1}{\epsilon_{\rm UV}}-\frac{1}{\epsilon_{\rm IR}}\ .\tag{4.13}$$

The UV pole in Γ contributes to the renormalization constant Z_2 and eventually leads to the correct running of the coupling constant.

E. Correction to the hard-scattering amplitude

The hard-scattering amplitude T_H for the process $\gamma\gamma\to M^+M^-$ is obtained as follows. One first computes Δ, the amplitude for the parton subprocess $\gamma\gamma\to(q\bar{q})+(q\bar{q})$. Since the virtuality of external particles and all masses are taken to be zero, this amplitude is gauge invariant. Then, using the distribution amplitude for the free quarks, T_H is obtained by rewriting the full amplitude in a factorized form as in Eq. (1.1). In this way, collinear singularities are systematically removed from T_H, leaving a well-defined expansion in α_s.

In order to extract T_H from Δ in a gauge-invariant way, we employ the method used in the calculation of the correction to the hard-scattering amplitude for the pion electromagnetic form factor.[4,5] The method consists in using dimensional regularization with massless on-shell quarks to regulate collinear singularities.

Since we are interested in obtaining the $T_H^{(1)}$ term in the expansion (1.2) for T_H, we have to compute $\Delta^{(1)}$. Contributing diagrams are shown in Figs. 7—10. Evaluating all the diagrams, we find that the total contribution is of the form

$$\begin{aligned}\Delta^{(1)}(x,y;\theta_{\rm c.m.})=\Delta^{(1)}_{\rm fin}(x,y;\theta_{\rm c.m.})\\ +\Delta^{(1)}_{\rm UV}(x,y;\theta_{\rm c.m.})\frac{1}{\hat{\epsilon}_{\rm UV}}\\ +\Delta^{(1)}_{\rm coll}(x,y;\theta_{\rm c.m.})\frac{1}{\hat{\epsilon}_{\rm IR}}\ .\end{aligned}\tag{4.14}$$

In a calculation as tedious as this one, it is important to have as many internal checks as possible. One very important check is to see that the third term on the right-hand side of (4.14) is such that it can be absorbed into the meson distribution amplitude. Use of the collinear Ward identities can be made to show that this nontrivial requirement is met by our final result.

Therefore, the one-loop hard-scattering amplitude, which we denote by $\overline{T}_H^{(1)}$, is obtained from (4.14) simply by leaving the third term out. Thus,

$$\overline{T}_H^{(1)}(x,y;\theta_{\rm c.m.})=\Delta^{(1)}_{\rm fin}(x,y;\theta_{\rm c.m.})+\Delta^{(1)}_{\rm UV}(x,y;\theta_{\rm c.m.})\frac{1}{\hat{\epsilon}_{\rm UV}}\ .\tag{4.15}$$

Let X be any of the four lowest-order diagrams of Fig. 5, and X_i a one-loop diagram generated from X by inserting an internal gluon line. Further, let $[X]$ and $[X_i]$ be a class of lowest-order diagrams and one-loop diagrams obtained from X and X_i, respectively, by particle interchange and by crossing the two photon vertices. Finally, let $\overline{T}_H^{(1)}[X_i]$ be the contribution of $[X_i]$ to $\overline{T}_H^{(1)}$. Then, we can write

$$\overline{T}_H^{(1)}[X_i]=\alpha_s T_H^{(0)}[X]\left[\frac{\alpha_s}{\pi}\right]\hat{T}_H^{(1)}[X_i]\ ,\tag{4.16}$$

where $T_H^{(0)}[X]$ is the contribution of $[X]$ to T_H, given by (3.10). For the purpose of this calculation, we use the simplest form for the meson distribution amplitude, namely, $\Phi_M=\delta(x-\frac{1}{2})$. Our hope is that like in the lowest-order case, the next-to-leading-order predictions for $\gamma\gamma\to M^+M^-$ will not be too sensitive to the precise form of $\Phi_M(x,Q)$. The only reason why the calculation is not done with the general form of $\Phi_M(x,Q)$ is that the already extensive labor involved would increase by, at least, a factor of 5.

Contributions to $\hat{T}_H^{(1)}$ arising from the diagrams of groups A, B, C, and D (shown in Figs. 7—10) for different photon helicity combinations and four values of the center-of-mass scattering angle (45°, 60°, 75°, and 90°) are listed in Tables I, II, III, and IV, respectively. (The numerical uncertainties quoted are 2-standard-deviation errors as estimated by VEGAS.) In these tables we use the notation

$$\zeta=-2+(\tfrac{5}{3}+2\ln 2)\frac{\beta_0}{4}\ ,\tag{4.17}$$

where β_0 is the first term in the perturbative expansion of the QCD β function, given by

$$\beta_0=11-\tfrac{2}{3}n_f\ ,\tag{4.18}$$

with n_f being the number of active quark flavors. On the basis of the results summarized in Tables I–IV, we find that

$$\hat{T}_H^{(1)}(\lambda\lambda';\theta_{\text{c.m.}})=\frac{\beta_0}{4}\left[\frac{1}{\hat{\epsilon}_{\text{UV}}}+(\tfrac{5}{3}+2\ln 2)\right]+\mathscr{F}(\lambda\lambda';\theta_{\text{c.m.}})\,, \qquad (4.19)$$

where

$$\left.\begin{matrix}\mathscr{F}(++;\theta_{\text{c.m.}})\\ \mathscr{F}(--;\theta_{\text{c.m.}})\end{matrix}\right\}=-\begin{cases}3.274(4), & \theta_{\text{c.m.}}=45^\circ\,,\\ 3.638(4), & \theta_{\text{c.m.}}=60^\circ\,,\\ 3.849(5), & \theta_{\text{c.m.}}=75^\circ\,,\\ 4.233(5), & \theta_{\text{c.m.}}=90^\circ\,,\end{cases} \qquad (4.20\text{a})$$

and

$$\left.\begin{matrix}\mathscr{F}(+-;\theta_{\text{c.m.}})\\ \mathscr{F}(-+;\theta_{\text{c.m.}})\end{matrix}\right\}=-\begin{cases}2.859(3), & \theta_{\text{c.m.}}=45^\circ\,,\\ 3.845(4), & \theta_{\text{c.m.}}=60^\circ\,,\\ 4.714(4), & \theta_{\text{c.m.}}=75^\circ\,,\\ 5.186(5), & \theta_{\text{c.m.}}=90^\circ\,.\end{cases} \qquad (4.20\text{b})$$

Therefore, the complete unrenormalized $\alpha_s{}^2$ result for the hard-scattering amplitude is

$$\hat{T}_H(\lambda\lambda';\theta_{\text{c.m.}})=T_H^{(0)}(\lambda\lambda';\theta_{\text{c.m.}})\times\alpha_s\left[1+\left[\frac{\alpha_s}{\pi}\right]\hat{T}_H^{(1)}(\lambda\lambda';\theta_{\text{c.m.}})\right], \qquad (4.21)$$

where $T_H^{(0)}(\lambda\lambda';\theta_{\text{c.m.}})$ is the lowest-order hard-scattering amplitude given by (3.10) with $x=y=\frac{1}{2}$.

We now proceed to renormalize the UV poles in (4.21) using the $\overline{\text{MS}}$ renormalization scheme. Renormalization is carried out by stating that the α_s appearing in (4.21) is the bare unrenormalized coupling related to the renormalized physical coupling $\alpha_{\overline{\text{MS}}}(W_{\gamma\gamma})$ by

$$\alpha_s=\alpha_{\overline{\text{MS}}}(W_{\gamma\gamma})\left[1-\frac{\alpha_{\overline{\text{MS}}}(W_{\gamma\gamma})}{\pi}\frac{\beta_0}{4}\left[\frac{1}{\hat{\epsilon}_{\text{UV}}}\right]\right]. \qquad (4.22)$$

Substituting this in (4.21), we get

TABLE I. Contribution to $\hat{T}_H^{(1)}$ of the diagrams shown in Fig. 7.

Class of diagrams	$\lambda\lambda'$	$\theta_{\text{c.m.}}$				Coefficient of $1/\hat{\epsilon}_{\text{UV}}$
		45°	60°	75°	90°	
A1	+ +	−2.376(1)	−1.980(1)	−1.700(1)	−1.591(1)	
	+ −	−2.376(1)	−1.980(1)	−1.700(1)	−1.591(1)	$-\frac{2}{3}$
A2	+ +	0	0	0	0	$-\frac{2}{3}$
	+ −					
A3	+ +	ζ	ζ	ζ	ζ	$\frac{1}{4}(\beta_0-6)$
	+ −					
A4	+ +	−0.347(2)	−0.287(2)	−0.248(1)	−0.233(1)	$-\frac{1}{24}$
	+ −	−0.351(2)	−0.296(1)	−0.258(1)	−0.246(1)	
A5	+ +	6.004(3)	5.358(4)	5.158(4)	5.131(2)	$-\frac{9}{8}$
	+ −	5.378(3)	4.358(4)	3.797(5)	3.605(1)	
A6	+ +	−5.469(2)	−5.433(2)	−5.522(2)	−5.580(1)	$\frac{2}{3}$
	+ −	−5.025(1)	−4.633(2)	−4.356(2)	−4.247(1)	
A7	+ +	0.714(1)	0.781(1)	0.849(1)	0.881(1)	$-\frac{1}{24}$
	+ −	0.630(1)	0.630(1)	0.630(1)	0.630(1)	
A8	+ +	−1.886(1)	−2.086(1)	−2.291(1)	−2.386(1)	$\frac{9}{8}$
	+ −	−1.636(1)	−1.636(1)	−1.636(1)	−1.636(1)	
A9	+ +	3.432(6)	4.147(3)	4.863(3)	5.180(1)	
	+ −	2.885(4)	2.970(4)	3.043(5)	3.069(2)	
A10	+ +	0.650(1)	0.336(1)	0.110(1)	0.020(1)	
	+ −	0.650(1)	0.336(1)	0.110(1)	0.020(1)	
A11	+ +	−1.139(5)	−0.698(5)	−0.453(3)	−0.361(1)	
	+ −	−1.166(7)	−0.705(4)	−0.427(3)	−0.318(1)	
A12	+ +	3.047(6)	1.545(6)	0.498(8)	0.123(7)	
	+ −	3.412(6)	2.216(6)	1.403(6)	1.114(7)	
A13	+ +	0.848(9)	0.474(4)	0.276(5)	0.216(7)	
	+ −	0.922(6)	0.455(6)	0.154(5)	0.048(3)	
A14	+ +	−1.285(4)	−0.775(2)	−0.420(3)	−0.289(3)	
	+ −	−1.208(4)	−0.636(2)	−0.218(3)	−0.058(3)	
A15	+ +	3.689(8)	3.098(10)	2.647(8)	2.494(4)	
	+ −	−0.348(7)	−0.551(7)	−0.592(9)	−0.626(6)	

$$\tilde{T}_H(\lambda\lambda';\theta_{\text{c.m.}})=T_H^{(0)}(\lambda\lambda';\theta_{\text{c.m.}})\alpha_{\overline{\text{MS}}}(W_{\gamma\gamma})\left[1+\frac{\alpha_{\overline{\text{MS}}}(W_{\gamma\gamma})}{\pi}\left[\frac{\beta_0}{4}(\tfrac{5}{3}+2\ln 2)+\mathscr{F}(\lambda\lambda';\theta_{\text{c.m.}})\right]\right] . \tag{4.23}$$

In the next step we remove the explicit dependence of (4.23) on n_f by introducing a new coupling constant $\bar{\alpha}(W_{\gamma\gamma})$, which is[21]

$$\bar{\alpha}(W_{\gamma\gamma})=\frac{\alpha_{\overline{\text{MS}}}(W_{\gamma\gamma})}{1-(\beta_0/4)(\tfrac{5}{3}+2\ln 2)\alpha_{\overline{\text{MS}}}(W_{\gamma\gamma})/\pi}=\alpha_{\overline{\text{MS}}}(W^*_{\gamma\gamma}) , \tag{4.24a}$$

where

$$W^*_{\gamma\gamma}=0.21\,W_{\gamma\gamma} \tag{4.24b}$$

is then the coupling-constant scale appropriate for the process in question. On the basis of (4.24), Eq. (4.23) can now be written as

$$T_H(\lambda\lambda';\theta_{\text{c.m.}})=T_H^{(0)}(\lambda\lambda';\theta_{\text{c.m.}})\alpha_{\overline{\text{MS}}}(W^*_{\gamma\gamma})\left[1+\frac{\alpha_{\text{MS}}(W^*_{\gamma\gamma})}{\pi}T_H^{(1)}(\lambda\lambda';\theta_{\text{c.m.}})\right] , \tag{4.25a}$$

TABLE II. Contribution to $\hat{T}_H^{(1)}$ of the diagrams shown in Fig. 8.

Class of diagrams	$\lambda\lambda'$	$\theta_{\text{c.m.}}$ 45°	60°	75°	90°	Coefficient of $1/\hat{\epsilon}_{\text{UV}}$
B1	+ +	−1.442(1)	−1.074(1)	−0.864(1)	−0.795(1)	$-\frac{1}{3}$
	+ −	−1.442(1)	−1.074(1)	−0.864(1)	−0.795(1)	
B2	+ +	−0.564(1)	−0.564(1)	−0.564(1)	−0.564(1)	$-\frac{1}{3}$
	+ −	−0.564(1)	−0.564(1)	−0.564(1)	−0.564(1)	
B3	+ +	0	0	0	0	$-\frac{2}{3}$
	+ −					
B4	+ +	ζ	ζ	ζ	ζ	$\frac{1}{4}(\beta_0-6)$
	+ −					
B5	+ +	1.107(2)	0.777(2)	0.592(1)	0.529(1)	$\frac{1}{3}$
	+ −	0.926(2)	0.582(1)	0.398(1)	0.345(1)	
B6	+ +	−3.928(1)	−3.606(1)	−3.431(1)	−3.371(1)	$\frac{1}{3}$
	+ −	0.080(1)	0.052(1)	0.015(1)	0.001(1)	
B7	+ +	0.065(1)	0.065(1)	0.065(1)	0.065(1)	$-\frac{1}{24}$
	+ −	0.065(1)	0.065(1)	0.065(1)	0.065(1)	
B8	+ +	1.428(1)	1.428(1)	1.428(1)	1.428(1)	$\frac{9}{8}$
	+ −	1.428(1)	1.428(1)	1.428(1)	1.428(1)	
B9	+ +	−0.886(1)	−0.886(1)	−0.886(1)	−0.886(1)	$\frac{9}{8}$
	+ −	−0.886(1)	−0.886(1)	−0.886(1)	−0.886(1)	
B10	+ +	0.140(1)	0.140(1)	0.140(1)	0.140(1)	$-\frac{1}{24}$
	+ −	0.140(1)	0.140(1)	0.140(1)	0.140(1)	
B11	+ +	0.077(3)	0.077(2)	0.076(2)	0.082(2)	
	+ −	−0.509(3)	−0.522(3)	−0.525(3)	−0.535(1)	
B12	+ +	−0.049(1)	−0.014(1)	0.001(1)	0.003(1)	
	+ −	−0.148(1)	−0.100(1)	−0.078(1)	−0.072(1)	
B13	+ +	−0.007(1)	−0.007(1)	−0.007(1)	−0.007(1)	
	+ −	−0.007(1)	−0.007(1)	−0.007(1)	−0.007(1)	
B14	+ +	−0.407(1)	−0.407(1)	−0.407(1)	−0.407(1)	
	+ −	−0.407(1)	−0.407(1)	−0.407(1)	−0.407(1)	
B15	+ +	0.061(1)	0.033(2)	0.026(2)	0.019(2)	
	+ −	0.599(2)	0.470(1)	0.406(1)	0.384(1)	
B16	+ +	3.689(3)	3.098(3)	2.647(3)	2.494(2)	
	+ −	−0.348(13)	−0.551(6)	−0.592(12)	−0.626(3)	
B17	+ +	−0.267(3)	−0.209(2)	−0.153(2)	−0.108(2)	
	+ −	−0.701(2)	−0.568(2)	−0.493(2)	−0.458(2)	
B18	+ +	0.888(9)	0.820(5)	0.804(4)	0.803(3)	
	+ −	0.888(9)	0.820(5)	0.804(4)	0.803(3)	

TABLE III. Contribution to $\hat{T}_H^{(1)}$ of the diagrams shown in Fig. 9.

Class of diagrams	$\lambda\lambda'$	$\theta_{\text{c.m.}}$				Coefficient of $1/\hat{\epsilon}_{\text{UV}}$
		45°	60°	75°	90°	
C1	+ +	−1.419(1)	−1.210(1)	−1.246(1)	−1.258(1)	$-\frac{2}{3}$
	+ −	−1.419(1)	−1.210(1)	−1.246(1)	−1.258(1)	
C2	+ +	0	0	0	0	$-\frac{2}{3}$
	+ −					
C3	+ +	ζ	ζ	ζ	ζ	$\frac{1}{4}(\beta_0-6)$
	+ −					
C4	+ +	−3.142(3)	−3.008(2)	−2.934(1)	−2.914(1)	$\frac{2}{3}$
	+ −	−3.142(2)	−3.008(2)	−2.934(1)	−2.914(1)	
C5	+ +	−0.206(1)	−0.098(1)	−0.046(1)	−0.032(1)	$-\frac{1}{12}$
	+ −	−0.102(1)	−0.052(1)	−0.034(1)	−0.032(1)	
C6	+ +	4.052(2)	3.900(2)	3.842(2)	3.856(2)	$\frac{9}{4}$
	+ −	4.052(2)	3.900(2)	3.842(2)	3.856(2)	
C7	+ +	0.219(1)	0.182(1)	0.167(1)	0.166(1)	
	+ −	0.219(1)	0.182(1)	0.167(1)	0.166(1)	
C8	+ +	0.613(1)	0.433(1)	0.338(1)	0.308(1)	
	+ −	0.151(1)	0.241(1)	0.292(1)	0.308(1)	
C9	+ +	0.202(1)	0.182(1)	0.174(1)	0.176(1)	
	+ −	0.336(1)	0.300(1)	0.284(1)	0.286(1)	
C10	+ +	−5.328(25)	−2.190(14)	−1.145(8)	−0.867(8)	
	+ −	−6.708(21)	−2.124(8)	−0.218(4)	0.488(4)	
C11	+ +	−0.771(21)	−0.324(14)	−0.221(10)	−0.195(3)	
	+ −	0.771(21)	−0.324(14)	−0.221(10)	−0.195(3)	
C12	+ +	6.757(17)	4.170(9)	3.209(7)	2.951(7)	
	+ −	6.624(15)	4.024(7)	3.061(5)	2.814(5)	
C13	+ +	−0.930(2)	−0.716(2)	−0.617(2)	−0.589(2)	
	+ −	−0.240(2)	−0.154(2)	−0.109(1)	−0.096(1)	

TABLE IV. Contribution to $\hat{T}_H^{(1)}$ of the diagrams shown in Fig. 10.

Class of diagrams	$\lambda\lambda'$	$\theta_{\text{c.m.}}$				Coefficient of $1/\hat{\epsilon}_{\text{UV}}$
		45°	60°	75°	90°	
D1	+ +	−1.230(1)	−0.896(1)	−0.721(1)	−0.667(1)	$-\frac{2}{3}$
	+ −	−1.452(1)	−1.056(1)	−0.775(1)	−0.667(1)	
D2	+ +	0	0	0	0	$-\frac{2}{3}$
	+ −					
D3	+ +	ζ	ζ	ζ	ζ	$\frac{1}{4}(\beta_0-6)$
	+ −					
D4	+ +	−4.537(2)	−4.109(2)	−3.876(1)	−3.802(1)	$\frac{2}{3}$
	+ −	−5.029(3)	−4.632(3)	−4.351(2)	−4.243(1)	
D5	+ +	−0.513(1)	−0.291(1)	−0.193(1)	−0.167(1)	$-\frac{1}{12}$
	+ −	−0.808(1)	−0.580(1)	−0.466(1)	−0.439(1)	
D6	+ +	0.124(1)	−0.011(1)	−0.123(1)	−0.531(1)	$\frac{9}{4}$
	+ −	1.543(2)	1.444(2)	1.279(2)	1.163(2)	
D7	+ +	2.593(2)	1.904(2)	1.546(2)	1.414(1)	
	+ −	2.931(2)	2.068(2)	1.481(2)	1.233(2)	
D8	+ +	−0.141(1)	−2.09(1)	−0.264(1)	−0.286(1)	
	+ −	−0.088(1)	−0.199(1)	−0.333(1)	−0.392(4)	
D9	+ +	1.012(4)	0.792(2)	0.685(1)	0.658(1)	
	+ −	1.230(3)	0.981(4)	0.818(3)	0.768(3)	
D10	+ +	−0.628(8)	−0.211(8)	−0.013(7)	−0.033(7)	
	+ −	−1.238(9)	−0.736(13)	−0.301(12)	−0.104(16)	

where

$$T_H^{(1)}(\lambda\lambda';\theta_{\text{c.m.}}) \equiv \mathcal{F}(\lambda\lambda';\theta_{\text{c.m.}}) , \tag{4.25b}$$

which is our final expression for the next-to-leading order hard-scattering amplitude.

F. Beyond leading-order predictions for the $\gamma\gamma \to M^+M^-$ cross section

Having obtained the hard-scattering amplitude in the preceding subsection, the next thing we need to get the $\gamma\gamma \to M^+M^-$ cross section is the helicity amplitude $\mathcal{M}(\lambda\lambda';\theta_{\text{c.m.}})$. According to (1.1), this amplitude is given as a convolution of the hard-scattering amplitude with the meson distribution amplitude Φ_M. This convolution, however, with the meson distribution amplitude of the form $\Phi_M = \delta(x-\frac{1}{2})$ has already been performed since in the evaluation of the diagrams contributing to T_H we have been using $x=y=\frac{1}{2}$ from the very beginning. Therefore, from (4.25) we find that the $\gamma\gamma \to M^+M^-$ process is, to order $\alpha_s{}^2$, described by the helicity amplitude

$$\mathcal{M}(\lambda\lambda';\theta_{\text{c.m.}}) = \mathcal{M}^{(0)}(\lambda\lambda';\theta_{\text{c.m.}})\alpha_{\overline{\text{MS}}}(W_{\gamma\gamma}^*)\left[1+\frac{\alpha_{\overline{\text{MS}}}(W_{\gamma\gamma}^*)}{\pi}\mathcal{M}^{(1)}(\lambda\lambda';\theta_{\text{c.m.}})\right] , \tag{4.26a}$$

with

$$\mathcal{M}^{(1)}(\lambda\lambda';\theta_{\text{c.m.}}) \equiv \mathcal{F}(\lambda\lambda';\theta_{\text{c.m.}}) . \tag{4.26b}$$

Here $\mathcal{M}^{(0)}(\lambda\lambda';\theta_{\text{c.m.}})$ is the lowest-order helicity amplitude which is of the form (3.12) with $x=y=\frac{1}{2}$.

In order to remove some dependence of (4.26) on the form of the meson distribution amplitude, here, just as in the lowest-order case, one can utilize the similarity of the $\gamma\gamma \to M^+M^-$ process with the timelike pion electromagnetic form factor $\gamma^* \to M^+M^-$.

There exist two independent next-to-leading order perturbative QCD calculations of the pion form factor, one by Field *et al.*[4] and the other by Dittes and Radyshkin.[5] Unfortunately, these two calculations are not in agreement with each other (and a third calculation is clearly necessary). For the purpose of this work we adhere to the calculation of Ref. 5. Using their result for the unrenormalized hard-scattering amplitude, setting $x=y=\frac{1}{2}$, and following the steps used in going from (4.21) to (4.24), we find that the pion form factor, to order $\alpha_s{}^2$, is given by

$$\overline{F}_M(s) = F_M^{(0)}(s)\alpha_{\overline{\text{MS}}}(W_{\gamma\gamma}^*)\left[1-2.33\frac{\alpha_{\overline{\text{MS}}}(W_{\gamma\gamma}^*)}{\pi}\right] , \tag{4.27}$$

where $F_M^{(0)}(s)$ is the lowest-order expression obtained from (3.11). In view of (4.26) and (4.27), we can now write

$$\mathcal{M}(\lambda\lambda';s,\theta_{\text{c.m.}}) = F_M(s)\left[\frac{\mathcal{M}^{(0)}(\lambda\lambda';s,\theta_{\text{c.m.}})}{F_M^{(0)}(s)}\right]\left[\frac{1+[\alpha_{\overline{\text{MS}}}(W_{\gamma\gamma}^*)/\pi]\mathcal{M}^{(1)}(\lambda\lambda';\theta_{\text{c.m.}})}{1-2.33[\alpha_{\overline{\text{MS}}}(W_{\gamma\gamma}^*)/\pi]}\right] . \tag{4.28}$$

Introducing the notation

$$\mathcal{P}^{(1)}(\lambda\lambda';\theta_{\text{c.m.}}) = [\mathcal{M}^{(0)}(\lambda\lambda';\theta_{\text{c.m.}})]^2\mathcal{M}^{(1)}(\lambda\lambda';\theta_{\text{c.m.}}) , \tag{4.29}$$

the next-to-leading-order spin-averaged differential cross section for the $\gamma\gamma \to M^+M^-$ reaction can be

$$\left[\frac{d\sigma}{dt}\right] = \left[\frac{d\sigma}{dt}\right]^{(0)}\left[1+\frac{\alpha_{\overline{\text{MS}}}(W_{\gamma\gamma}^*)}{\pi}h(\theta_{\text{c.m.}})\right] , \tag{4.30a}$$

where $(d\sigma/dt)^{(0)}$ is given by (3.15) with $\rho(z,\Phi_M)=1$, and

$$h(\theta_{\text{c.m.}}) = 2\left[2.333+\frac{\mathcal{P}^{(1)}(++,\theta_{\text{c.m.}})+\mathcal{P}^{(1)}(+-,\theta_{\text{c.m.}})}{|\mathcal{M}^{(0)}(++,\theta_{\text{c.m.}})|^2+|\mathcal{M}^{(0)}(+-;\theta_{\text{c.m.}})|^2}\right] = -\begin{cases} 1.575(2), & \theta_{\text{c.m.}}=45^\circ , \\ 2.744(3), & \theta_{\text{c.m.}}=60^\circ , \\ 3.480(3), & \theta_{\text{c.m.}}=75^\circ , \\ 4.255(4), & \theta_{\text{c.m.}}=90^\circ . \end{cases} \tag{4.30b}$$

Now, in order to see how the correction to the lowest-order prediction for the $\gamma\gamma \to M^+M^-$ differential cross section depends on the center-of-mass energy of the $\gamma\gamma$ system, in Fig. 11 we plot the ratio $R_{\text{diff}}=(d\sigma/dt)/(d\sigma/dt)^{(0)}$ for three different values of $W_{\gamma\gamma}$. Curves *a*, *b*, and *c* correspond to $W_{\gamma\gamma}=2$, 5, and 10 GeV, respectively. We take $\Lambda_{\overline{\text{MS}}}=150$ MeV.

Integrating (4.30) over the angular range determined by

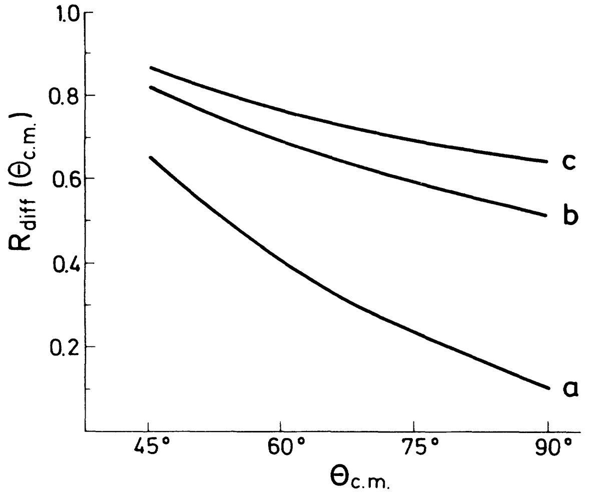

FIG. 11. Plot of $R_{\rm diff}$ vs $\theta_{\rm c.m.}$ for three different values of $W_{\gamma\gamma}$. Curves a, b, and c correspond to $W_{\gamma\gamma}=2$, 5, and 10 GeV, respectively.

$|\cos\theta_{\rm c.m}| < \delta$, we find that

$$\frac{\sigma}{\sigma^{(0)}}(\delta, W_{\gamma\gamma}) \equiv R_{\rm int}(\delta, W_{\gamma\gamma})$$

$$= 1 - f(\delta)\frac{\alpha_{\overline{\rm MS}}(W^*_{\gamma\gamma})}{\pi} . \tag{4.31a}$$

Here the function $f(\delta)$, the graph of which is shown in Fig. 12, is given by

$$f(\delta) = \frac{\int_{-\delta}^{+\delta} g(z)h(z)dz}{\int_{-\delta}^{+\delta} g(z)dz} , \tag{4.31b}$$

where

$$g(z) = \frac{1}{(1-z^2)^2} - \frac{4}{9}\frac{1}{1-z^2} + \frac{8}{9} \tag{4.31c}$$

is the function obtained from the expression inside the large parentheses in (3.15) by setting $e_1 = \frac{2}{3}$, $e_2 = -\frac{1}{3}$, and $\rho(z,\Phi_M) = 1$, while

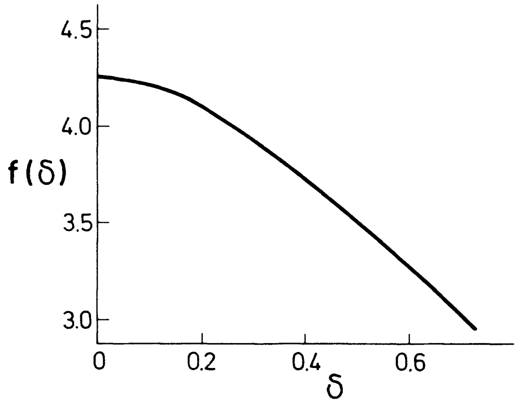

FIG. 12. Graph of the function $f(\delta)$.

$$h(z) = 4.255 - 14.709z^2 + 50.373z^4 - 63.353z^6 \tag{4.31d}$$

is the fit of the function defined numerically by (4.30b). The $W_{\gamma\gamma}$ dependence of the ratio $R_{\rm int}$, defined by (4.31), is shown in Fig. 13 for three different values of the parameter δ. Curves a, b, and c correspond to $\delta = 0.1$, 0.2, and 0.3, respectively.

Equations (4.30) and (4.31), represented graphically in Figs. 11 and 13, are the main result of this work. A glance at these figures reveals that the corrections to the lowest-order results become sufficiently small ($<25\%$) only for $W_{\gamma\gamma} > 10$ GeV.

The processes $\gamma\gamma \to M^+M^-$ ($M = \pi, K$) have been the subject of a number of experimental investigations. Measurements of $\sigma(\gamma\gamma\to\pi^+\pi^- + K^+K^-)$ in the region $1.6 \le W_{\gamma\gamma} \le 2.4$ GeV and the angular range confined to $|\cos\theta_{\rm c.m.}| < 0.3$ have been made by the Mark II group at SPEAR (Ref. 15). These measurements have then been extended to include the region $2.4 \le W_{\gamma\gamma} \le 3.5$ GeV (Ref. 16). Using the PEP4/9 detector at the SLAC e^+e^- storage ring PEP, separate contributions in the same region of $W_{\gamma\gamma}$ and the angular range given by $|\cos\theta_{\rm c.m.}| < 0.6$ have now been obtained.[17] Figures 14 and 15 show the PEP4/9 data for the $\gamma\gamma\to\pi^+\pi^-$ and $\gamma\gamma\to K^+K^-$ integrated cross sections, respectively, and their $W_{\gamma\gamma}$ dependence in comparison with the leading-

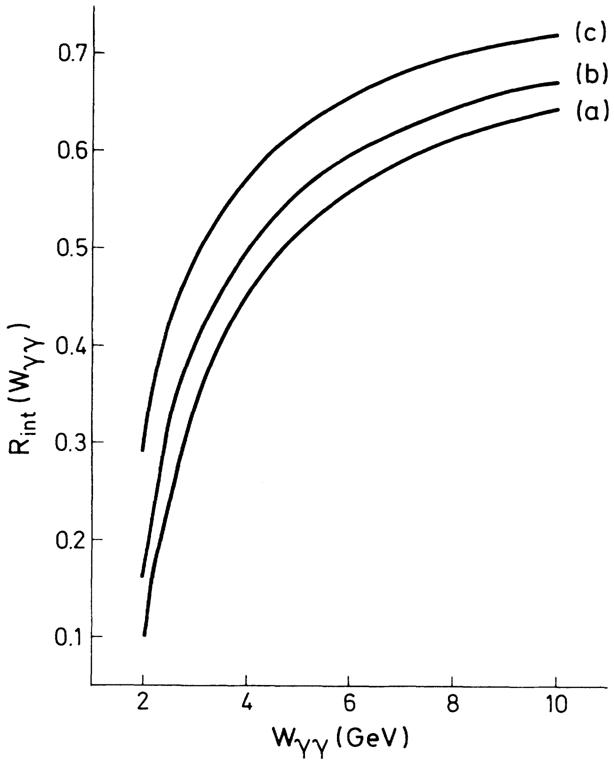

FIG. 13. $W_{\gamma\gamma}$ dependence of $R_{\rm int}$ for three different values of the parameter δ. Curves (a), (b), and (c) correspond to $\delta = 0.1$, 0.3, and 0.5, respectively.

(solid curves) and next-to-leading-order (dashed curves) perturbative QCD calculations.

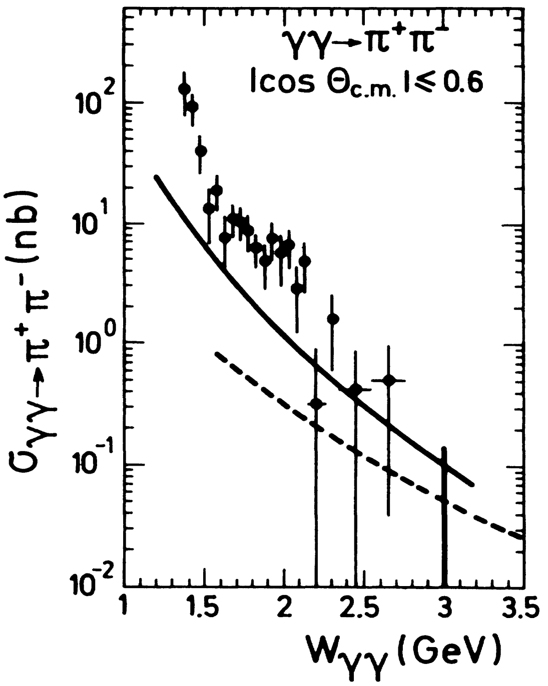

FIG. 14. PEP4/9 data for the $\gamma\gamma\to\pi^+\pi^-$ cross section compared with the leading-order (solid curve) and the next-to-leading-order (dashed curve) perturbative QCD predictions.

From Fig. 14 one sees that the $W_{\gamma\gamma}$ dependence of the $\gamma\gamma\to\pi^+\pi^-$ cross-section data is only in fair agreement with the calculation of Brodsky and Lepage. The lack of agreement can possibly be ascribed to the interference of the continuum with the $f(1270)$ and other resonances, completely or incompletely reconstructed as $\pi^+\pi^-$ final states.[17] On the other hand, as is seen from Fig. 15, the K^+K^- data are in very good agreement, in both the $W_{\gamma\gamma}$ dependence and the absolute normalization, with the lowest-order QCD prediction. As to the next-to-leading-order predictions, one sees that they deviate considerably from both the $\pi^+\pi^-$ and the K^+K^- data, indicating unreliability of the perturbative calculation in the region of $W_{\gamma\gamma}$ in which the data exist.

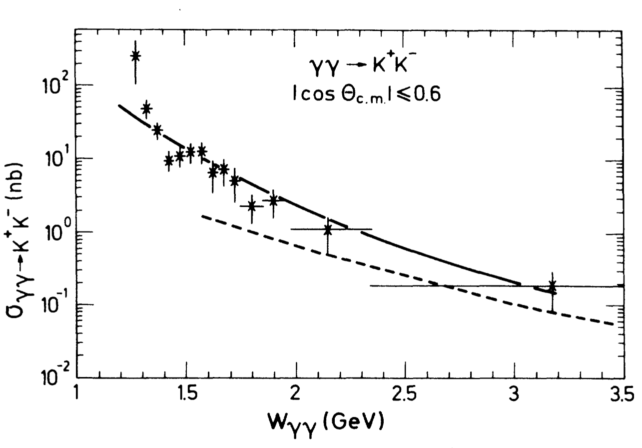

FIG. 15. PEP4/9 data for the $\gamma\gamma\to K^+K^-$ cross section compared with the leading-order (solid curve) and the next-to-leading-order (dashed curve) perturbative QCD predictions.

V. CONCLUSION

Taking into account the contributions from 448 one-loop Feynman diagrams, the next-to-leading-order perturbative QCD predictions have been obtained for the $\gamma\gamma\to M^+M^-$ ($M=\pi,K$) transitions at large momentum transfer. The model meson distribution amplitude $\Phi_M\propto\delta(x-\frac{1}{2})$ has been utilized as a candidate form for the nonperturbative dynamical input. The correction to the evolution kernel for the meson distribution amplitude (which is needed to obtain complete next-to-leading-order prediction) has not been taken into account. This is certainly not a crude approximation since it is known that most of the $W_{\gamma\gamma}$ dependence of necessary helicity amplitudes comes from the hard-scattering amplitude and that the meson distribution amplitude varies slowly with changing $W_{\gamma\gamma}$. With the aim of reducing the effect of the special form of Φ_M chosen, similarity between $\gamma\gamma\to M^+M^-$ and $\gamma^*\to M^+M^-$ has been employed. In the $\overline{\text{MS}}$-scheme definition of α_s (renormalized at $W_{\gamma\gamma}$) and with the present estimate for $\Lambda_{\overline{\text{MS}}}$ (~ 150 MeV), corrections to the lowest-order predictions are found to become sufficiently small ($<25\%$) only for $W_{\gamma\gamma}>10$ GeV, which is much larger than the highest $W_{\gamma\gamma}$ for which experimental data exist.

Because of the particular form of Φ_M used in the calculation, some uncertainty has probably been brought into the predictions obtained. The size of this uncertainty is not easy to guess without doing the calculations with different forms of Φ_M. However, we know that the lowest-order predictions for the $\gamma\gamma\to M^+M^-$ reaction are almost completely independent of Φ_M if the similarity between this reaction and $\gamma^*\to M^+M^-$ is taken into account. Our hope is (and it is not unreasonable to expect) that something similar happens in the next-to-leading order also, and that the predictions obtained are not too sensitive to the precise forms of the meson distribution amplitude Φ_M.

In summary, the results of the analysis which has been carried out in this paper indicate that reliable perturbative predictions for the $\gamma\gamma\to M^+M^-$ ($M=\pi,K$) process cannot be made until $W_{\gamma\gamma}$ of 10 GeV is reached or unless higher-order terms in the perturbative expansion are obtained.

ACKNOWLEDGMENTS

I wish to thank Professor G. P. Lepage for his suggestion of this problem and his guidance throughout the work. I also gratefully acknowledge many helpful discussions with Professor Hikaru Kawai.

APPENDIX A

To illustrate the calculational method, in this appendix we present a detailed evaluation of diagram A14 of Fig. 7.

Using the momentum assignments shown in Fig. 16, the contribution of this diagram, to, say, the $T(++)$ helicity amplitude can be written as

$$T_{\mathrm{A}14}(++)=e_q{}^2g^4\left[\frac{4}{s}\left[-\frac{2}{9}\right]\right]I\ , \tag{A1}$$

where e_q is the electric charge of the quark line to which the photons are attached, g is the strong coupling constant, $-\frac{2}{9}$ is the color factor for the diagram, and I is the loop integral given by

$$I=\frac{1}{i}(\mu^2)^{-\epsilon}\int\frac{d^nl}{(2\pi)^n}\frac{N}{D_1D_2D_3D_4D_5D_0}\ . \tag{A2}$$

The numerator in (A2) is of the form

$$N=\mathrm{Tr}\left[\left[\frac{\gamma_5\not{P}_{M^+}}{\sqrt{2}}\right]\gamma^\nu\not{p}_1\not{\epsilon}_1^+\not{p}_2\gamma^\mu\not{p}_3\not{\epsilon}_2^+\times\left[\frac{\gamma_5\not{P}_{M^-}}{\sqrt{2}}\right]\gamma_\nu\not{p}_4\gamma_\mu\right]\ , \tag{A3}$$

where

$$P_{M^+}=p+k,\ \ P_{M^-}=p-k\ ,$$
$$p_1=\frac{p+k}{2}-l,\ \ p_2=-\frac{p}{2}-q+\frac{k}{2}-l\ , \tag{A4}$$
$$p_3=\frac{p}{2}-q+\frac{k}{2}-l,\ \ p_4=\frac{p-k}{2}+l\ .$$

The momenta p, q, and k and the polarization vectors ϵ_1^+ and ϵ_2^+ are defined in (2.2) and (2.3), respectively. The six denominators in (A2) are

$$D_1=l^2+i0,\ \ D_2=\left[l-\frac{p+k}{2}\right]^2+i0\ ,$$
$$D_3=\left[l+\frac{p-k}{2}\right]^2+i0,\ \ D_4=\left[l+\frac{p}{2}+q-\frac{k}{2}\right]^2+i0\ , \tag{A5}$$
$$D_5=(l+p)^2+i0,\ \ D_0=\left[\frac{p}{2}-q+\frac{k}{2}\right]^2\ .$$

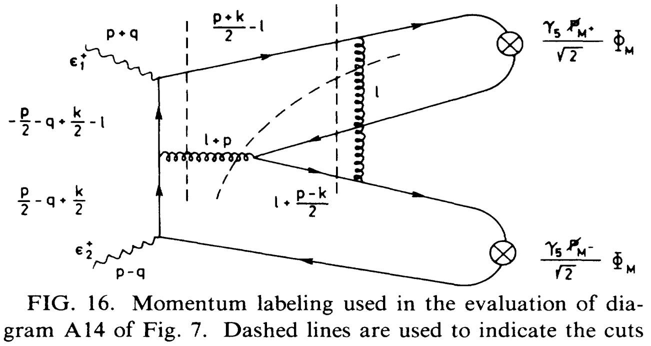

FIG. 16. Momentum labeling used in the evaluation of diagram A14 of Fig. 7. Dashed lines are used to indicate the cuts present in the diagram.

A glance at these denominators (or at Fig. 16) reveals that the integral I contains one soft and three collinear divergences. These divergences come from the following regions for the virtual-gluon momenta:

$$\begin{aligned}&\text{region A: } l \text{ soft}\ ,\\ &\text{region B: } l\,||\,(p+k)\ ,\\ &\text{region C: } l\,||\,(p-k)\ ,\\ &\text{region D: } (l+p)\,||\,(p+k)\ .\end{aligned} \tag{A6a}$$

In terms of the light-cone variables, where $l=(l^+,l^-,l_\perp)$, the above four integration regions can be characterized as

$$\begin{aligned}&\text{region A: } l_\mu\to 0(\mu=+,-,\perp)\ ,\\ &\text{region B: } l^+\gg l^-,l_\perp\ ,\\ &\text{region C: } l^-\gg l^+,l_\perp\ ,\\ &\text{region D: } (l+p)^+\gg(l+p)^-,(l+p)\perp\ .\end{aligned} \tag{A6b}$$

Let l_{A}, l_{B}, l_{C}, and l_{D} be the limiting form of the loop momentum vector l in the regions A, B, C, and D, respectively. Then, in view of (A6), we have

$$l_{\mathrm{A}}=0\ , \tag{A7a}$$

$$l_{\mathrm{B}}=\frac{l^+}{2}(p+k)\ , \tag{A7b}$$

$$l_{\mathrm{C}}=\frac{l^-}{2}(p-k)\ , \tag{A7c}$$

$$l_{\mathrm{D}}=-p+\frac{(l+p)^+}{2}(p+k)\ . \tag{A7d}$$

Since the integral I is beset by singularities and is too complicated to be evaluated analytically, we proceed as follows. We first define the subtraction terms (or counterterms) $I_{\mathrm{IR}}^{\mathrm{A}}$, $I_{\mathrm{coll}}^{\mathrm{B}}$, $I_{\mathrm{coll}}^{\mathrm{C}}$, and $I_{\mathrm{coll}}^{\mathrm{D}}$ which approximate the original integral I in the regions A, B, C, and D, respectively. Let us denote by I_{ST} the sum of all subtraction terms, i.e.,

$$I_{\mathrm{ST}}=I_{\mathrm{IR}}^{A}+I_{\mathrm{coll}}^{B}+I_{\mathrm{coll}}^{\mathrm{C}}+I_{\mathrm{coll}}^{\mathrm{D}}\ . \tag{A8}$$

Then, the integral I can formally be written as

$$I=(I-I_{\mathrm{ST}})+I_{\mathrm{ST}}\ . \tag{A9}$$

The point of writing I in this form lies in that the first term on the right-hand side is finite by construction, while all the singularities of the original integral are now separated and contained in the second term. Equation (A9) can also be written as

$$I=I_{\mathrm{fin}}^{(1)}+(I_{\mathrm{fin}}^{(2)}+I_{\mathrm{div}})\ , \tag{A10}$$

where $I_{\mathrm{fin}}^{(1)}=I-I_{\mathrm{ST}}$, while $I_{\mathrm{fin}}^{(2)}$ and I_{div} stand for the finite and divergent part of I_{ST}, respectively. We evaluate $I_{\mathrm{fin}}^{(1)}$ numerically (in four dimensions). On the other hand, $I_{\mathrm{fin}}^{(2)}$ is obtained by computing I_{ST} in n space-time dimensions, expanding the result in the Laurent series around $n=4$, taking the limit $n\to 4$, and keeping the terms that remain finite in this limit. The sum of the pole terms then corresponds to I_{div}.

We now proceed to construct the subtraction terms explicitly. Since the soft divergence coming from the region A overlaps with the collinear divergences coming from the regions B and C, we start by subtracting the soft divergence first. This is done by simply setting $l=l_A$ in the numerator and in the denominators D_4 and D_5 of the original integral I, i.e.,

$$I_{\rm IR}^{\rm A}=\int\frac{d^nl}{(2\pi)^n}\frac{N_{\rm A}}{D_1D_2D_3D_{4\rm A}D_{5\rm A}D_0}\ . \qquad (\rm A11)$$

Subtracting (A11) from (A2), we obtain

$$I-I_{\rm IR}^{\rm A}=\int\frac{d^nl}{(2\pi)^n}\frac{N-N_{\rm A}D_4D_5/D_{4\rm A}D_{5A}}{D_1D_2D_3D_4D_5D_0}\ . \qquad (\rm A12)$$

This integral is now finite when $l\to 0$, but still contains all three collinear divergences. Our next step is to construct collinear subtraction terms. The subtraction term $I_{\rm coll}^{\rm B}$ is obtained by substituting $l=l_B$ in the numerator and in D_3 and D_4 in the denominator of (A12). Thus

$$I_{\rm coll}^{\rm B}=\int\frac{d^nl}{(2\pi)^n}\frac{N_{\rm B}-N_{\rm A}D_{4\rm B}D_{5\rm B}/D_{4\rm A}D_{5\rm A}}{D_1D_2D_{3\rm B}D_{4B}D_5D_0}\ . \qquad (\rm A13)$$

Similarly, the subtraction term $I_{\rm coll}^{\rm C}$ is constructed by setting $l=l_{\rm C}$ in the numerator and in D_2 and D_5 in the denominator of (A12). The result is

$$I_{\rm coll}^{\rm C}=\int\frac{d^nl}{(2\pi)^n}\frac{N_{\rm C}-N_{\rm A}D_{4\rm C}D_{5\rm C}/D_{4\rm A}D_{5\rm A}}{D_1D_{2\rm C}D_3D_4D_{5\rm C}D_0}\ . \qquad (\rm A14)$$

On the other hand, since the collinear divergence from the region D does not overlap with the soft divergence, the corresponding collinear subtraction term $I_{\rm coll}^{\rm D}$ is obtained by simply setting $l=l_{\rm D}$ in the numerator and in D_1 and D_5 in the denominator in (A2), giving

$$I_{\rm coll}^{\rm D}=\int\frac{d^nl}{(2\pi)^n}\frac{N_{\rm D}}{D_{1\rm D}D_2D_3D_4D_{5\rm D}D_0}\ . \qquad (\rm A15)$$

Performing in (A11)–(A15) the necessary γ-matrix algebra, in n space-time dimensions, and introducing the notation $z=\cos\theta_{\rm c.m.}$, we find that the subtraction terms are

$$I_{\rm IR}^{\rm A}=-\left[\left[\frac{1+z}{1-z}\right]-\left[\frac{3-z}{1-z}\right]\epsilon_{\rm IR}\right]\int\frac{d^nl}{(2\pi)^n}\frac{1}{D_1D_2D_3}\ , \qquad (\rm A16)$$

$$I_{\rm coll}^{\rm B}=\left[\left[\frac{1+z}{1-z}\right]-\left[\frac{3-z}{1-z}\right]\epsilon_{\rm IR}\right]\int\frac{d^nl}{(2\pi)^n}\frac{1}{D_1D_2D_5}\ , \qquad (\rm A17)$$

$$I_{\rm coll}^{\rm C}=\left[\frac{1+z}{1-z}\right](\epsilon_{\rm IR}-z)\int\frac{d^nl}{(2\pi)^n}\frac{1}{D_1D_3D_4}\ , \qquad (\rm A18)$$

$$I_{\rm coll}^{\rm D}=(1+z)(1+\epsilon_{\rm IR})\int\frac{d^nl}{(2\pi)^n}\frac{1}{D_2D_3D_{4\rm D}D_5}\ , \qquad (\rm A19a)$$

where

$$D_{4\rm D}=-zl^+-1+i0\ . \qquad (\rm A19b)$$

In the expressions (A11)–(A19) the factor $-i(\mu^2)^{-\epsilon}$ has been systematically suppressed. On the basis of (A9), (A10), and (A16)–(A19) we find that

$$I_{\rm fin}^{(1)}=\frac{1}{i}\int\frac{d\mathbf{l}\,dl_0}{(2\pi)^4}\left[\frac{N-(1+z)D_4D_5}{D_1D_2D_3D_4D_5D_0}-\left[\frac{1+z}{1-z}\right]\left[\frac{1}{D_1D_2D_3}-\frac{z}{D_1D_3D_4}+\frac{1-z}{D_2D_3D_{4\rm D}D_5}\right]\right]\ , \qquad (\rm A20)$$

with

$$N=2l[(1-z^2)\cos\theta+z(1-z^2)^{1/2}\sin\theta\cos\theta]-(1-z^2)\ , \qquad (\rm A21)$$

where l is the magnitude and θ and ϕ are the polar angles of the loop three-momentum vector $\mathbf{l}$. We next perform the l_0 integration using the method of residues. Let $l_0^{(i)}$ be the pole of the denominator D_i ($i=1,2,3,4,4{\rm D},5$). Then, closing the integration contour in the lower l_0 half-plane, we find that the contributing (enclosed) poles are

$$\begin{aligned} l_0^{(1)}&=l-i0\ ,\\ l_0^{(2)}&=\tfrac{1}{2}+(l^2-l\cos\theta+\tfrac{1}{4})^{1/2}-i0\ ,\\ l_0^{(3)}&=-\tfrac{1}{2}+(l^2-l\cos\theta+\tfrac{1}{4})^{1/2}-i0\ ,\\ l_0^{(4)}&=-\tfrac{1}{2}+(l^2-l+\tfrac{5}{4})^{1/2}-i0\ ,\\ l_0^{(5)}&=l-1-i0\ , \end{aligned} \qquad (\rm A22)$$

where

$$a=(1-2z)\cos\theta+2(1-z^2)^{1/2}\sin\theta\cos\phi\ . \qquad (\rm A23)$$

Carrying out the l_0 integration, we arrive at the three-momentum integral which is a sum of 15 terms. A typical term is of the form

$$\int\frac{d\mathbf{l}}{(2\pi)^3}\frac{F(l_0=l_0^{(j)})}{D_{1j}D_{2j}\cdots D_{5j}}\ , \qquad (\rm A24)$$

where $D_{ij}(l)$ is the denominator D_i evaluated at the pole of the denominator D_j, i.e., $D_{ij}(l)=D_i(l_0=l_0^{(j)})$. At this point it is very important to examine the pole structure of the integrand. Suppose that there exists l_{ij} such that $0<l_{ij}<\infty$ and $D_{ij}(l_{ij})=0$. This means that there is an ij cut, i.e., propagators i and j can go on shell simultaneously. Examining all D_{ij}'s, we find three such cuts, namely,

$$\begin{aligned} D_{32}(l)&=1-2(l^2-l\cos\theta+\tfrac{1}{4})^{1/2}\ ,\\ D_{51}(l)&=1-2l\ ,\\ D_{52}(l)&=2-3l\cos\theta\ , \end{aligned} \qquad (\rm A25)$$

which vanish for

$$l_{32}=|\cos\theta|\,,\ \ l_{51}=\tfrac{1}{2},\ \ l_{52}=\frac{2}{3-\cos\theta}\ , \qquad (\rm A26)$$

respectively. Since the integral contains the (first-order) poles given by (A26), it is properly defined by the principal-value prescription which amounts to using the identity

$$\frac{1}{D_{ij}(l)+i0}=P\frac{1}{D_{ij}(l)}-i\pi\frac{\delta(l-l_{ij})}{|D'_{ij}(l)|_{l=l_{ij}}} , \qquad \text{(A27)}$$

for each D_{ij} in (A25). As a result of this the integral splits into two parts, a real part and an imaginary part. Since the lowest-order amplitude is real, the imaginary part of the amplitude at the one-loop level will not contribute (to the order in α_s that we are interested in), so we just drop it. As far as the integral representing the real part is concerned, it is not yet ready for numerical integration. Before putting it on computer, it is very important to perform a transformation on the integrand, so that a local cancellation of infinities, coming from the opposite sides of a pole, is achieved. An efficient way of doing this is described in detail in Appendix B. After this is carried out, the final integration is easily performed. The result is

$$I^{(1)}_{\text{fin}}=\begin{cases}-0.680(9), & \theta_{\text{c.m.}}=45^\circ ,\\ -0.130(3), & \theta_{\text{c.m.}}=60^\circ ,\\ 0.051(3), & \theta_{\text{c.m.}}=75^\circ ,\\ 0.103(3), & \theta_{\text{c.m.}}=90^\circ .\end{cases} \qquad \text{(A28)}$$

We now proceed to evaluate all the subtraction terms analytically. This requires evaluating the loop integrals in (A16)–(A19) and is performed using the standard methods. The subtraction term I^{A}_{IR} is given by

$$I^{\text{A}}_{\text{IR}}=\frac{1}{(4\pi)^2}\left[\frac{C_2(z)}{\epsilon_{\text{IR}}{}^2}+\frac{C_1(z)}{\epsilon_{\text{IR}}}+C_0(z)\right] . \qquad \text{(A29)}$$

Since all the soft singularities cancel out when all the diagrams are put together, explicit expressions for $C_{0,1,2}(z)$ are not needed and we do not give them here. It is, however, interesting to mention that I^{A}_{IR} has a divergent imaginary part [$C_0(z)$ and $C_1(z)$ are imaginary]. This is related to the fact that $l_{32}=|\cos\theta|$ can be equal to zero.

The collinear subtraction terms are of the form

$$I^{i}_{\text{coll}}=\frac{1}{(4\pi)^2}\left[F_i(z)\frac{1}{\hat{\epsilon}_{\text{IR}}}+G_i(z)\right] \quad (i=\text{B,C,D}) , \qquad \text{(A30)}$$

where

$$F_{\text{B}}(z)=-\left[\frac{1+z}{1-z}\right]\ln 2 ,$$

$$G_{\text{B}}(z)=-\left[\left[\frac{3-z}{1-z}\right]-\left[\frac{1+z}{1-z}\right]\right]\ln 2 ; \qquad \text{(A31)}$$

$$F_{\text{C}}(z)=\left[\frac{1+z}{1-z}\right]\ln(1-z) ,$$

$$G_{\text{C}}(z)=\left[\frac{1+z}{1-z}\right]\left[\frac{1}{z}-\frac{\ln(1-z)}{2}\right]\ln(1-z) ; \qquad \text{(A32)}$$

$$F_{\text{D}}(z)=-\ln\left[\frac{1+z}{2}\right] ,$$

$$G_{\text{D}}(z)=-(1+z)[K_1(z)+K_2(z)] ; \qquad \text{(A33)}$$

with

$$K_1(z)=\int_0^1 dy\frac{1+\ln(1+y)}{(1+y)(1-yz)},\quad K_2(z)=\int_0^1 dx\int_0^1 dy\frac{1}{(1-x)(1+y)}\left[\frac{1}{1+(1-x(1+y))z}-\frac{1}{1-yz}\right] . \qquad \text{(A34)}$$

On the basis of (A31)–(A34) we get

$$I^{(2)}_{\text{fin}}=-\begin{cases}0.197(1), & \theta_{\text{c.m.}}=45^\circ ,\\ 0.079(1), & \theta_{\text{c.m.}}=60^\circ ,\\ 0.039(1), & \theta_{\text{c.m.}}=75^\circ ,\\ 0.021(1), & \theta_{\text{c.m.}}=90^\circ .\end{cases} \qquad \text{(A35)}$$

Combining now (A28) and (A35), we find that the finite part of I is given by

$$I_{\text{fin}}=\begin{cases}-0.877(9), & \theta_{\text{c.m.}}=45^\circ ,\\ -0.209(3), & \theta_{\text{c.m.}}=60^\circ ,\\ 0.012(3), & \theta_{\text{c.m.}}=75^\circ ,\\ 0.082(3), & \theta_{\text{c.m.}}=90^\circ .\end{cases} \qquad \text{(A36)}$$

On the other hand, in view of (A30)–(A33), the divergent part of I is

$$I_{\text{div}}=I^{\text{A}}_{\text{IR}}+\frac{1}{(4\pi)^2}\left[\sum_i F_i(z)\right]\frac{1}{\hat{\epsilon}_{\text{IR}}} \quad (i=B,C,D) . \qquad \text{(A37)}$$

This completes our evaluation of diagram A14 of Fig. 7.

APPENDIX B

In this appendix we present a method suitable for numerical evaluation of the integrals containing first-order poles and are, therefore, properly defined by the principal-value prescription. For simplicity of notation and with no loss of generality, we restrict ourselves to one-dimensional integrals.

To begin with, consider the following integral:

$$J_1=\int_{x_{\min}}^{x_{\max}} dx\frac{f(x)}{x-a},\quad x_{\min}<a<x_{\max} . \qquad \text{(B1)}$$

Since this integral has a single pole, it is defined by the principal-value prescription, i.e.,

$$J_1 = \lim_{\epsilon \to 0} \left[\int_{x_{\min}}^{a-\epsilon} dx \frac{f(x)}{x-a} + \int_{a+\epsilon}^{x_{\max}} dx \frac{f(x)}{x-a} \right] . \tag{B2}$$

Introducing new integration variables by

$$y_1 = \frac{x - x_{\min}}{a - x_{\min}}, \quad y_2 = \frac{x_{\max} - x}{x_{\max} - a} , \tag{B3}$$

into the first and second terms in (B2), respectively, we obtain

$$\begin{aligned} J_1 = \lim_{\epsilon \to 0} \Bigg[& \int_0^{1-\epsilon/(a-x_{\min})} dy_1 \frac{f(g_{\min}(y_1))}{y_1 - 1} \\ & + \int_{1-\epsilon/(x_{\max}-a)}^{0} dy_2 \frac{f(g_{\max}(y_2))}{y_2 - 1} \Bigg] , \end{aligned} \tag{B4}$$

where

$$\begin{aligned} g_{\min}(y) &= x_{\min} + (a - x_{\min}) y , \\ g_{\max}(y) &= x_{\max} + (a - x_{\max}) y . \end{aligned} \tag{B5}$$

Equation (B4) can now be written in the form

$$\begin{aligned} J_1 = & \int_0^1 dy \frac{f(g_{\min}(y))}{y-1} + \int_1^0 dy \frac{f(g_{\max}(y))}{y-1} \\ & - \lim_{\epsilon \to 0} \Bigg[\int_{1-\epsilon/(a-x_{\min})}^{1} dy \frac{f(g_{\min}(y))}{y-1} \\ & \qquad - \int_{1-\epsilon/(x_{\max}-a)}^{1} dy \frac{f(g_{\max}(y))}{y-1} \Bigg] . \end{aligned} \tag{B6}$$

Denoting the sum of the first two terms by J_1^* and introducing a new integration variable $z = y - 1$ into the last two integrals, (B6) becomes

$$\begin{aligned} J_1 = J_1^* + \lim_{\epsilon \to 0} \Bigg[& \int_0^{-\epsilon/(a-x_{\min})} \frac{dz}{z} f(g_{\min}(1+z)) \\ & + \int_{-\epsilon/(x_{\max}-a)}^{0} \frac{dz}{z} f(g_{\max}(1+z)) \Bigg] , \end{aligned} \tag{B7}$$

which, in the $\epsilon \to 0$ limit, takes the form

$$J_1 = J_1^* + f(a) \int_{-\epsilon/(x_{\max}-a)}^{-\epsilon/(a-x_{\min})} \frac{dz}{z} , \tag{B8}$$

or, finally,

$$J_1 = J_1^* + f(a) \ln \left[\frac{x_{\max} - a}{a - x_{\min}} \right] . \tag{B9}$$

Here $f(a)$ is the residue of the integrand at the pole a. The second term in (B9) is a "correction term" which appears owing to the fact that

$$\left. \frac{dy_1(x)}{dx} \right|_{x=a} \neq - \left. \frac{dy_2(x)}{dx} \right|_{x=a} , \tag{B10}$$

where y_1 and y_2 are the integration variables in the integration regions 1 and 2, respectively.

At first sight, nothing has been achieved in going from (B1) to (B9); the original integral has been replaced by another (nothing simpler) integral plus an extra term. The important point to observe, however, is that unlike in the case of the original integral J_1, which is finite owing to a nonlocal cancellation of infinite contributions (coming from the opposite sides of the pole), the integral J_1^* is finite because the integrand is now finite at each point of the integration region. This is crucial if one wants to evaluate the integral J_1 numerically. Rewriting J_1 in the form (B9) amounts to a folding of the integration region around the pole, as a result of which the infinities fall on top of each other and cancel out.

Let us now apply the above procedure to the integral containing n first-order poles:

$$J_n = \int_{x_{\min}}^{x_{\max}} dx \frac{f(x)}{(x-a_1)(x-a_2) \cdots (x-a_n)} . \tag{B11}$$

In order to prepare this integral for numerical evaluation we first divide the integration region into $n+1$ subregions

$$[x_{\min}, x_{\max}] = [x_{\min}, a_1] \cup [a_1, a_2] \cup \cdots \cup [a_n, x_{\max}]$$

and represent (B11) as

$$J_n = \lim_{\epsilon \to 0} \sum_{k=1}^{n+1} \int_{a_{k-1}+c_{k-1}\epsilon}^{a_k - c_k \epsilon} dx\, F(x) , \tag{B12}$$

where

$$a_0 = x_{\min}, \quad a_{n+1} = x_{\max} \tag{B13a}$$

and

$$c_k = (1 - \delta_{k-1,0})(1 - \delta_{k,n+1}) . \tag{B13b}$$

Introducing a new integration variable into the kth term (integral) in (B12) by

$$y_k = \frac{a_k - a_{k-1} + (-1)^k (a_k + a_{k-1} - 2x)}{2(a_k - a_{k-1})} , \tag{B14}$$

yields

$$J_n = \sum_{k=1}^{n+1} (-1)^k (a_k - a_{k-1}) \int_{Z_{k-1}}^{Z_k} dy_k F(G(y_k)) , \tag{B15a}$$

where

$$G(y_k) = \tfrac{1}{2} [(a_k + a_{k-1}) + (-1)^k (a_k - a_{k-1})(1 - y_k)] \tag{B15b}$$

and

$$\begin{aligned} Z_{k-1} &= \frac{1+(-1)^k}{2} + (-1)^{k+1} \frac{a_{k-1}}{a_k - a_{k-1}} \epsilon , \\ Z_k &= \frac{1+(-1)^{k+1}}{2} + (-1)^k \frac{a_k}{a_k - a_{k-1}} \epsilon . \end{aligned} \tag{B15c}$$

Equation (B15) may be written as

$$J_n = J_n^* + \Delta J_n , \tag{B16}$$

where

$$J_n^* = \sum_{k=1}^{n+1} (-1)^k (a_k - a_{k-1}) \int_{\omega_{k-1}}^{\omega_k} dy_k F(G(y_k)) \tag{B17a}$$

and

$$\omega_k=\frac{1+(-1)^k}{2}\ . \tag{B17b}$$

The second term on the right-hand side of (B16) is given by the expression

$$\Delta J_n=\sum_{k=1}^{n}\operatorname{Res}F(a_k)\ln\left|\frac{a_{k+1}-a_k}{a_k-a_{k-1}}\right|\ . \tag{B18}$$

All the integrals in (B17) diverge; the first integral at the upper limit, the last one at the lower limit, while all the others diverge at both limits. Note, however, that the divergence of the kth integral at the lower (upper) limit is canceled by the divergence of the $(k-1)$th[$(k+1)$th] integral at the upper [lower] limit. Thus, J_n is now finite owing to a local cancellation of infinities. The term J_n in (B16), given by (B18), does not present any problem and is easily evaluated. Its origin is related to the fact that

$$\left.\frac{dy_k}{dx}\right|_{x=a_k}\neq-\left.\frac{dy_{k+1}}{dx}\right|_{x=a_k}\quad(k=1,2,\ldots,n)\ . \tag{B19}$$

Therefore, having represented J_n in the form given by (B16)—(B19), our goal has been achieved. The integral J_n is now ready to be evaluated numerically.

We now proceed to present a slightly modified version of the method described above. The only difference is that now instead of the linear change of variables, given by (B14), we use a nonlinear one, namely,

$$y_k=\begin{cases}\dfrac{x}{a_1}, & \text{for } k=1\ ,\\[2ex] \dfrac{1+(-1)^k}{2}+\dfrac{s_k(a_k-a_{k-1})(x-a_{k-1})}{(a_k-a_{k-1})-(x-a_{k-1})[1+(-1)^k(a_k-a_{k-1})s_k]}, & \text{for } k=2,3,\ldots,n+1\ ,\end{cases} \tag{B20}$$

where

$$s_k=\begin{cases}\dfrac{1}{a_1}, & \text{for } k=1\ ,\\[2ex] -\dfrac{1}{a_1}, & \text{for } k=2\ ,\\[2ex] -\left.\dfrac{dy_k}{dx}\right|_{x=a_{k-1}}, & \text{for } k=3,4,\ldots,n+1\ .\end{cases} \tag{B21}$$

It may be seen from (B20) and (B21) that s_k satisfies the following recursion relation:

$$s_k=-\frac{1}{s_{k-1}(a_{k-1}-a_{k-2})^2}\quad(k=3,4,\ldots,n+1)\ . \tag{B22}$$

On the basis of (B20)—(B22) it is easily verified that we now have

$$\left.\frac{dy_k}{dx}\right|_{x=a_k}=-\left.\frac{dy_{k+1}}{dx}\right|_{x=a_k}\ . \tag{B23}$$

Because of this, the integral J_n can, in terms of new integration variables, be represented as

$$J_n=\sum_{k=1}^{n+1}\int_{\omega_{k-1}}^{\omega_k}dy_k j_k F[x=x(y_k)]\ , \tag{B24}$$

where

$$j_k=\left[\frac{dy_k}{dx}\right]^{-1}=\begin{cases}a_1, & \text{for } k=1\ ,\\[2ex] \dfrac{s_k(a_k-a_{k-1})^2}{\{(a_k-a_{k-1})+[1+(-1)^k(a_k-a_{k-1})s_k](x-a_{k-1})\}^2}, & \text{for } k=2,\ldots,n+1\ ,\end{cases} \tag{B25}$$

is the Jacobian of the transformation (B20). Therefore, with use of the integration variables given by (B20), the "correction term" ΔJ_n, requiring the evaluation of the residues of the integrand, is absent. This makes the latter version of the method simpler and more efficient.

---

*Present address: Rudjer Bošković Institute, 41001 Zagreb, Yugoslavia.

[1] G. P. Lepage and S. J. Brodsky, Phys. Rev. D 22, 2157 (1980).

[2] A. V. Efremov and A. V. Radyushkin, Theor. Mat. Phys. **42**, 97 (1980).

[3] S. J. Brodsky and G. P. Lepage, *Quantum Chromodynamics*, proceedings of the Summer Workshop on Quantum Chromodynamics, edited by W. Frazer and F. Henyey (AIP Conf. Proc. No. 55) (AIP, New York, 1979); Phys. Lett. **87B**, 359 (1979); S. J. Brodsky, Y. Frishman, G. P. Lepage, and C.

Sachrajda, *ibid.* **91B**, 239 (1980); A. V. Efremov and A. V. Radyushkin, Rev. Nuovo Cimento **3**, 1 (1980); Phys. Lett. **94B**, 245 (1980); A. Duncan and A. Mueller, Phys. Rev. D **21**, 1636 (1980); Phys. Lett. **90B**, 159 (1980); G. R. Farrar and D. R. Jackson, Phys. Rev. Lett. **43**, 246 (1979); V. L. Chernyak and A. R. Zhitnitsky, Pis'ma Zh. Eksp. Teor. Fiz. **25**, 14 (1977) [JETP Lett. **25**, 11 (1977)]; G. Parisi, Phys. Lett. **43**, 43 (1979); M. K. Chase, Nucl. Phys. **B167**, 125 (1980).

[4] R. D. Field *et al.*, Nucl. Phys. **B168**, 429 (1981).

[5] F. M. Dittes and A. V. Radyushkin, Yad. Fiz. **34**, 529 (1981) [Sov. J. Nucl. Phys. **34**, 293 (1981)].

[6] P. V. Landshoff, Phys. Rev. D **10**, 1024 (1974); P. V. Landshoff and D. J. Pritchard, Z. Phys. C **6**, 69 (1980); A. Duncan and A. H. Mueller, Phys. Lett. **90B**, 159 (1980).

[7] G. P. Lepage and S. J. Brodsky, Phys. Rev. D **24**, 1808 (1980).

[8] P. H. Damgaard, Nucl. Phys. **B211**, 435 (1983); G. R. Farrar, E. Maina, and F. Neri, Rutgers Report No. RU-83-33, 1983 (unpublished); Rutgers Report No. RU-84-13, 1984 (unpublished); G. W. Atkinson, J. Sucher, and K. Tsokos, Phys. Lett. **137B**, 407 (1984).

[9] S. J. Brodsky and G. P. Lepage, Phys. Rev. D **24**, 2848 (1981); S. C. Chao, Nucl. Phys. **B195**, 381 (1982); H. F. Jones and J. Wyndham, *ibid.* **B195**, 222 (1984); K. Tsokos, Phys. Lett. **136B**, 429 (1984); A. Andrikopoulou, Z. Phys. C **22**, 63 (1984); P. H. Damgaard, K. Tsokos, and E. L. Berger, CERN Report No. CERN-TH.4112/85 (unpublished).

[10] V. L. Chernyak and A. R. Zhitnitsky, Nucl. Phys. **B201**, 492 (1982); V. L. Chernyak, A. R. Zhitnitsky, and I. R. Zhitnitsky, *ibid.* **B204**, 477 (1982); B. L. Ioffe and A. V. Smilga, *ibid.* **B216**, 373 (1983); V. L. Chernyak and A. R. Zhitnitsky, Phys. Rep. **112**, 173 (1984).

[11] M. Creutz, in *Perturbative Quantum Chromodynamics,* Tallahassee, 1981, edited by D. W. Duke and J. F. Owens (AIP, Conf. Proc. No. 74) (AIP, New York, 1981); H. R. Quinn and M. Weinstein, Phys. Rev. D **25**, 1661 (1982); D. Horn and M. Weinstein, *ibid.* **25**, 3331 (1982); R. Blankenbecler, D. J. Scalapino, and R. L. Sugar, *ibid.* **24**, 2778 (1981); J. E. Hirsh, D. J. Scalapino, R. L. Sugar, and R. Blankenbecler, Report No. NSF-ITP-81-89, 1981 (unpublished); S. Gottlieb and A. S. Kronfeld, Phys. Rev. D **33**, 227 (1986).

[12] S. Brodsky, T. Huang, and G. P. Lepage, in *Particles and Fields—2,* proceedings of the Banff Summer Institute, 1981, edited by A. Z. Capri and A. N. Kamal (Plenum, New York, 1983).

[13] V. M. Budnev *et al.*, Phys. Rep. **15**, 181 (1975).

[14] F. E. Low, Phys. Rev. **120**, 582 (1960); G. Bonneau, M. Gourdin, and F. Martin, Nucl. Phys. **B54**, 573 (1973).

[15] J. R. Smith *et al.*, Phys. Rev. D **30**, 851 (1984).

[16] G. Gidal, in *Multiparticle Dynamics 1985,* proceedings of the XVIth International Symposium, Kiryat-Anavim, Israel, 1985, edited by J. Greenhaus (World Scientific, Singapore, in press).

[17] J. C. Sens, Report No. SLAC-PUB-3754, 1985 (unpublished).

[18] Current data give $f_\pi = 93$ MeV and $f_K = 112$ MeV.

[19] A. C. Hearn, Stanford University Report No. ITP-247 (unpublished).

[20] G. P. Lepage, J. Comput. Phys. **27**, 192 (1978).

[21] S. J. Brodsky, G. P. Lepage, and P. B. Mackenzie, Phys. Rev. D **28**, 228 (1983).